

# Convective scale and subadiabatic layers in simulations of rotating compressible convection

P. J. Käpylä<sup>1,2</sup>

<sup>1</sup> Leibniz-Institute for Solar Physics (KIS), Schöneckstr. 6, D-79104 Freiburg, Germany email: [pkapyla@leibniz-kis.de](mailto:pkapyla@leibniz-kis.de)

<sup>2</sup> Georg-August-University Göttingen, Institute for Astrophysics and Geophysics, Friedrich-Hund-Platz 1, D-37077 Göttingen, Germany

October 20, 2023

## ABSTRACT

*Context.* Rotation is thought to influence the size of convective eddies and the efficiency of convective energy transport in the deep convection zones of stars. Rotationally constrained convection has been invoked to explain the lack of large-scale power in observations of solar flows.

*Aims.* The main aims are to quantify the effects of rotation on the scale of convective eddies and velocity, the depths of convective overshoot, and the subadiabatic Deardorff layers.

*Methods.* Moderately turbulent three-dimensional hydrodynamic simulations of rotating convection in local Cartesian domains were run. The rotation rate and luminosity of the simulations are varied to probe the dependency of the results on Coriolis, Mach, and Richardson numbers measuring the influences of rotation, compressibility, and stiffness of the radiative layer. The results were compared with theoretical scaling results that assume a balance between Coriolis, inertial, and buoyancy (Archimedean) forces, which is also referred to as the CIA balance.

*Results.* The horizontal scale of convective eddies decreases as rotation increases, and ultimately reaches a rotationally constrained regime consistent with the CIA balance. Using a new measure of the rotational influence on the system, it is shown that even the deep parts of the solar convection zone are not in the rotationally constrained regime. The simulations capture the slowly and rapidly rotating scaling laws predicted by theory, and the Sun appears to be in between these two regimes. Both, the overshooting depth and the extent of the Deardorff layer, decrease as rotation becomes more rapid. For sufficiently rapid rotation the Deardorff layer is absent due to the symmetrization of up- and downflows. However, for the most rapidly rotating cases the overshooting increases again due to unrealistically large Richardson numbers that allow convective columns penetrate deep into the radiative layer.

*Conclusions.* Relating the simulations with the Sun suggests that the convective scale even in the deep parts of the Sun is only mildly affected by rotation and that some other mechanism is needed to explain the lack of strong large-scale flows in the Sun. Taking the current results at face value, the overshoot and Deardorff layers are estimated to span roughly five per cent of the pressure scale height at the base of the convection zone in the Sun.

**Key words.** turbulence – convection

## 1. Introduction

The theoretical understanding of solar and stellar convection was shaken roughly a decade ago when helioseismic analysis suggested that the velocity amplitudes in the deep solar convection zone are orders of magnitude smaller than anticipated from theoretical and numerical models (Hanasoge et al. 2012). Significant effort has been put in refining these estimates but a gaping discrepancy between numerical models and helioseismology remains (e.g. Hanasoge et al. 2016; Proxauf 2021); see, however Greer et al. (2015). This issue is now referred to as the convective conundrum (O’Mara et al. 2016).

Several solutions to this conundrum have been proposed, including high effective Prandtl number (e.g. Karak et al. 2018), rotationally constrained convection (Featherstone & Hindman 2016), and that the superadiabatic layer in the Sun is much thinner than thus far thought (Brandenburg 2016); see also Käpylä et al. (2023) and references therein. The two latter ideas are explored further in the current study. The idea that convection is rotationally constrained in the deep convection zone (CZ) is already borne out of mixing length models of solar convection that imply velocity amplitudes  $u_{\text{conv}}$  of about  $10 \text{ m s}^{-1}$  for the

deep convection zone, while the convective length scale  $\ell_{\text{conv}}$ , which is the mixing length, is of the order of 100 Mm, yielding a Coriolis number  $\text{Co}_{\odot} = 2\Omega_{\odot}\ell_{\text{conv}}/u_{\text{conv}}$  of the order of 10 (e.g. Ossendrijver 2003; Schumacher & Sreenivasan 2020). However, this estimate does not take into account the decreasing length scale due to the rotational influence on convection. Assuming that the Coriolis, inertial, and buoyancy (Archimedean) forces balance, also known as the CIA balance (e.g. Stevenson 1979; Ingersoll & Pollard 1982; King & Buffett 2013; Barker et al. 2014; Aurnou et al. 2020; Vasil et al. 2021), implies that the convective scale is given by  $\ell_{\text{conv}} \propto \text{Co}^{-1/2}$ , where  $\text{Co} = 2\Omega H/u_{\text{conv}}$  is a global Coriolis number, where  $\Omega$  is the rotation rate and where  $H$  is a length scale corresponding to the system size (e.g. Aurnou et al. 2020). This idea has been explored recently by Featherstone & Hindman (2016) and Vasil et al. (2021) who suggested that the largest convectively driven scale in the Sun coincides with that of supergranulation due to rotationally constrained convection in the deep CZ. These studies assumed from the outset that convection is strongly rotationally affected. Here a somewhat different perspective is taken in that an attempt is made to assess whether this assumption holds for the deep solar CZ. Furthermore, in addition to  $\ell_{\text{conv}}$ , the scalings of various

quantities based on predictions from the CIA balance are studied over a wide range of rotation rates.

Simulations of stratified overshooting convection have revealed that deep parts of CZs are often weakly stably stratified (e.g. Roxburgh & Simmons 1993; Tremblay et al. 2015; Hotta 2017; Bekki et al. 2017; Käpylä et al. 2017; Käpylä 2019). This is interpreted such that convection is driven by the cooling at the surface that induces cool downflow plumes which pierce through the entire convection zone and penetrate deep into the stable layers below. This process has been named entropy rain (e.g. Brandenburg 2016) and goes back to ideas presented by Spruit (1997) and the simulations of Stein and Nordlund (e.g. Stein & Nordlund 1989, 1998). This picture of convection is a clean break from the canonical view in which convection is driven throughout the convection zone by a superadiabatic temperature gradient, an idea which is also encoded into the mixing length concept (e.g. Vitense 1953; Böhm-Vitense 1958). Theoretically this can be understood such that the convective energy flux that is traditionally proportional to the entropy gradient is supplemented by a non-gradient term proportional to the variance of entropy fluctuations (Deardorff 1961, 1966).

Analysis of the force balance of up- and downflows in non-rotating hydrodynamic simulations supports the idea of surface-driven non-local convection (e.g. Käpylä et al. 2017; Käpylä 2019, 2021). Thus far these studies have mostly concentrated on non-rotating convection (see, however Käpylä et al. 2019; Viviani & Käpylä 2021). Here rotation is included to study its impact on the formation and extent of stably stratified Deardorff layers where the convective flux runs counter to the entropy gradient. Another aspect of interest in astrophysics is convective overshooting (see, e.g. Anders & Pedersen 2023, for a recent review). Numerical studies targeting specifically overshooting have largely concentrated on non-rotating cases (e.g. Singh et al. 1995, 1998; Saikia et al. 2000; Brummell et al. 2002; Hotta 2017; Käpylä 2019; Anders et al. 2022), and the effects of rotation have received much less attention (e.g. Ziegler & Rüdiger 2003; Käpylä et al. 2004; Brun et al. 2017). It is generally thought that rotation leads to reduction of overshooting depth (e.g. Ziegler & Rüdiger 2003) but a comprehensive study of this is still lacking.

The remainder of the paper is organized as follows: the model is described in Section 2, whereas the results and conclusions of the study are presented in Sections 3 and 4, respectively. The derivations related to the CIA balance are presented in Appendix A.

## 2. The model

The model is the same as that used in Käpylä (2019, 2021). The PENCIL CODE (Pencil Code Collaboration et al. 2021)<sup>1</sup> was used to produce the simulations. Convection is modeled in a Cartesian box with dimensions  $(L_x, L_y, L_z) = (4, 4, 1.5)d$ , where  $d$  is the depth of the initially convectively unstable layer. The equations for compressible hydrodynamics are solved:

$$\frac{D \ln \rho}{Dt} = -\nabla \cdot \mathbf{u}, \quad (1)$$

$$\frac{D\mathbf{u}}{Dt} = \mathbf{g} - \frac{1}{\rho}(\nabla p - \nabla \cdot 2\nu\rho\mathbf{S}) - 2\boldsymbol{\Omega} \times \mathbf{u}, \quad (2)$$

$$T \frac{Ds}{Dt} = -\frac{1}{\rho} [\nabla \cdot (\mathbf{F}_{\text{rad}} + \mathbf{F}_{\text{SGS}}) - \mathcal{C}] + 2\nu\mathbf{S}^2, \quad (3)$$

where  $D/Dt = \partial/\partial t + \mathbf{u} \cdot \nabla$  is the advective derivative,  $\rho$  is the density,  $\mathbf{u}$  is the velocity,  $\mathbf{g} = -g\hat{e}_z$  is the acceleration due to gravity with  $g > 0$ ,  $p$  is the pressure,  $T$  is the temperature,  $s$  is the specific entropy,  $\nu$  is the constant kinematic viscosity, and  $\boldsymbol{\Omega} = \Omega_0(-\sin\theta, 0, \cos\theta)^T$  is the rotation vector, where  $\theta$  is the colatitude.  $\mathbf{F}_{\text{rad}}$  and  $\mathbf{F}_{\text{SGS}}$  are the radiative and turbulent subgrid scale (SGS) fluxes, respectively, and  $\mathcal{C}$  describes cooling near the surface.  $\mathbf{S}$  is the traceless rate-of-strain tensor with

$$S_{ij} = \frac{1}{2}(u_{i,j} + u_{j,i}) - \frac{1}{3}\delta_{ij}\nabla \cdot \mathbf{u}. \quad (4)$$

The gas is assumed to be optically thick and fully ionized, where radiation is modeled via the diffusion approximation. The ideal gas equation of state  $p = (c_P - c_V)\rho T = \mathcal{R}\rho T$  applies, where  $\mathcal{R}$  is the gas constant, and  $c_P$  and  $c_V$  are the specific heats at constant pressure and volume, respectively. The radiative flux is given by

$$\mathbf{F}_{\text{rad}} = -K\nabla T, \quad (5)$$

where  $K$  is the radiative heat conductivity

$$K = \frac{16\sigma_{\text{SB}}T^3}{3\kappa\rho}, \quad (6)$$

where  $\sigma_{\text{SB}}$  is the Stefan-Boltzmann constant and  $\kappa$  is the opacity. Assuming that the opacity is a power law of the form  $\kappa = \kappa_0(\rho/\rho_0)^a(T/T_0)^b$ , where  $\rho_0$  and  $T_0$  are reference values of density and temperature, the heat conductivity is

$$K(\rho, T) = K_0(\rho/\rho_0)^{-(a+1)}(T/T_0)^{3-b}. \quad (7)$$

The choice  $a = 1$  and  $b = -7/2$  corresponds to the Kramers opacity law (Weiss et al. 2004), which was used in convection simulations by Edwards (1990) and Brandenburg et al. (2000).

Additional turbulent SGS diffusivity is applied for the entropy fluctuations with

$$\mathbf{F}_{\text{SGS}} = -\rho T \chi_{\text{SGS}} \nabla s', \quad (8)$$

where  $s'(\mathbf{x}) = s(\mathbf{x}) - \bar{s}$  with the overbar indicating horizontal averaging. The coefficient  $\chi_{\text{SGS}}$  is constant in the whole domain and  $\mathbf{F}_{\text{SGS}}$  has a negligible contribution to the net energy flux such that  $\overline{\mathbf{F}_{\text{SGS}}} \approx 0$ .

The cooling at the surface is described by

$$\mathcal{C} = \rho c_P \frac{T_{\text{cool}} - T}{\tau_{\text{cool}}} f_{\text{cool}}(z), \quad (9)$$

where  $\tau_{\text{cool}}$  is a cooling time,  $T = e/c_V$  is the temperature where  $e$  is the internal energy, and where  $T_{\text{cool}} = T_{\text{top}}$  is a reference temperature corresponding to the fixed value at the top boundary.

The advective terms in Equations (1) to (3) are written in terms of a fifth-order upwinding derivative with a hyperdiffusive sixth-order correction with a local flow-dependent diffusion coefficient; see Appendix B of Dobler et al. (2006).

### 2.1. Geometry, initial and boundary conditions

The computational domain is a rectangular box where the vertical coordinate is  $z_{\text{bot}} \leq z \leq z_{\text{top}}$  with  $z_{\text{bot}}/d = -0.45$ ,  $z_{\text{top}}/d = 1.05$ . The horizontal coordinates  $x$  and  $y$  run from  $-2d$  to  $2d$ . The initial stratification consists of three layers. The two lower layers are polytropic with polytropic indices  $n_1 = 3.25$  ( $z_{\text{bot}}/d \leq z/d \leq 0$ ) and  $n_2 = 1.5$  ( $0 \leq z/d \leq 1$ ). The former follows from a radiative solution that is a polytrope with

<sup>1</sup> <https://github.com/pencil-code/>

index  $n = (3 - b)/(1 + a)$ ; see [Barekat & Brandenburg \(2014\)](#), Appendix A of [Brandenburg \(2016\)](#), and Figure 1. The latter corresponds to a marginally stable isentropic stratification. Initially the uppermost layer above  $z/d = 1$  is isothermal, mimicking a photosphere where radiative cooling is efficient. Convection ensues because the system is not in thermal equilibrium due to the cooling near the surface and due to the inefficient radiative diffusion in the layers above  $z/d = 0$ . The velocity field is initially seeded with small-scale Gaussian noise with amplitude  $10^{-5}\sqrt{d\bar{g}}$ .

The horizontal boundaries are periodic and the vertical boundaries are impenetrable and stress free according to

$$\frac{\partial u_x}{\partial z} = \frac{\partial u_y}{\partial z} = u_z = 0. \quad (10)$$

A constant energy flux is imposed at the lower boundary by setting

$$\frac{\partial T}{\partial z} = -\frac{F_{\text{bot}}}{K_{\text{bot}}}, \quad (11)$$

where  $F_{\text{bot}}$  is the fixed input flux and  $K_{\text{bot}} = K(x, y, z_{\text{bot}})$ . Constant temperature  $T = T_{\text{top}}$  is imposed on the upper vertical boundary.

## 2.2. Units and control parameters

The units of length, time, density, and entropy are given by

$$[x] = d, \quad [t] = \sqrt{d/g}, \quad [\rho] = \rho_0, \quad [s] = c_P, \quad (12)$$

where  $\rho_0$  is the initial value of density at  $z = z_{\text{top}}$ . The models are fully defined by choosing the values of  $\nu$ ,  $\Omega_0$ ,  $\theta$ ,  $g$ ,  $a$ ,  $b$ ,  $K_0$ ,  $\rho_0$ ,  $T_0$ ,  $\tau_{\text{cool}}$ , and the SGS Prandtl number

$$\text{Pr}_{\text{SGS}} = \frac{\nu}{\chi_{\text{SGS}}}, \quad (13)$$

along with the cooling profile  $f_{\text{cool}}(z)$ . The values of  $K_0$ ,  $\rho_0$ ,  $T_0$  are subsumed into another constant  $\bar{K}_0 = K_0\rho_0^{a+1}T_0^{b-3}$  which is fixed by assuming the radiative flux at  $z_{\text{bot}}$  to equal  $F_{\text{bot}}$  at  $t = 0$ . The cooling profile  $f_{\text{cool}}(z) = 1$  above  $z/d = 1$  and  $f_{\text{cool}}(z) = 0$  below  $z/d = 1$ , connecting smoothly across the interface over a width of  $0.025d$ . The quantity  $\xi_0 = H_{\text{p}}^{\text{top}}/d = \mathcal{R}T_{\text{top}}/gd$  sets the initial pressure scale height at the surface and determining the initial density stratification. All of the current simulations have  $\xi_0 = 0.054$ .

Prandtl number based on the radiative heat conductivity is

$$\text{Pr}(\mathbf{x}) = \frac{\nu}{\chi(\mathbf{x})}, \quad (14)$$

where  $\chi(\mathbf{x}) = K(\mathbf{x})/c_P\rho(\mathbf{x})$ , quantifies the relative importance of viscous to temperature diffusion. Unlike many other simulations, Pr is not an input parameter because of the non-linear dependence of the radiative diffusivity on the ambient thermodynamics. The dimensionless normalized flux is given by

$$\mathcal{F}_{\text{n}} = \frac{F_{\text{bot}}}{\rho(z_{\text{bot}})c_s^3(z_{\text{bot}})}, \quad (15)$$

where  $\rho(z_{\text{bot}})$  and  $c_s(z_{\text{bot}})$  are the density and the sound speed, respectively, at  $z = z_{\text{bot}}$  at  $t = 0$ . At the base of the solar CZ  $\mathcal{F}_{\text{n}} \approx 4 \cdot 10^{-11}$  (e.g. [Brandenburg et al. 2005](#)), whereas in the current fully compressible simulations several orders of magnitude larger values are used.

The effect of rotation is quantified by the Taylor number

$$\text{Ta} = \frac{4\Omega_0^2 d^4}{\nu^2}, \quad (16)$$

which is related to the Ekman number via  $\text{Ek} = \text{Ta}^{-1/2}$ .

The Rayleigh number based on the energy flux is given by

$$\text{Ra}_{\text{F}} = \frac{gd^4 F_{\text{bot}}}{c_P \rho T \nu \chi^2}. \quad (17)$$

This can be used to construct a flux-based diffusion-free modified Rayleigh number (e.g. [Christensen 2002](#); [Christensen & Aubert 2006](#))

$$\text{Ra}_{\text{F}}^* = \frac{\text{Ra}_{\text{F}}}{\text{Pr}^2 \text{Ta}^{3/2}}, \quad (18)$$

In the current set-up  $\text{Ra}_{\text{F}}^*$  is given by

$$\text{Ra}_{\text{F}}^* = \frac{gF_{\text{bot}}}{8c_P \rho T \Omega_0^3 d^2}. \quad (19)$$

A reference depth needs to be chosen because  $\text{Ra}_{\text{F}}^* = \text{Ra}_{\text{F}}^*(z)$ . Furthermore,  $\bar{H} \equiv c_P T/g$  is a length scale related to the pressure scale height. The choice  $d = \bar{H} = H_{\text{p}}$ , where  $H_{\text{p}} \equiv -(\partial \ln p / \partial z)^{-1}$  is the pressure scale height at the base of the convection zone, leads to

$$\text{Ra}_{\text{F}}^* = \frac{F_{\text{bot}}}{8\rho\Omega_0^3 H_{\text{p}}^3}. \quad (20)$$

## 2.3. Diagnostics quantities

The global Reynolds and SGS Péclet numbers describe the strength of advection versus viscosity and SGS diffusion

$$\text{Re} = \frac{u_{\text{rms}}}{\nu k_1}, \quad \text{Pe}_{\text{SGS}} = \frac{u_{\text{rms}}}{\chi_{\text{SGS}} k_1}, \quad (21)$$

where  $u_{\text{rms}}$  is the volume averaged rms-velocity, and where  $k_1 = 2\pi/d$  is an estimate of the largest eddies in the system. The Reynolds and Péclet number based on the actual convective length scale  $\ell$  are given by

$$\text{Re}_{\ell} = \frac{u_{\text{rms}}\ell}{\nu}, \quad \text{Pe}_{\ell} = \frac{u_{\text{rms}}\ell}{\chi_{\text{SGS}}}. \quad (22)$$

Here  $\ell = k_{\text{mean}}^{-1}$  is chosen, where  $k_{\text{mean}} = k_{\text{mean}}(z)$  is the mean wavenumber (e.g. [Christensen & Aubert 2006](#); [Schinnerer et al. 2012](#)), and which is computed from

$$k_{\text{mean}}(z) = \frac{\int k E(k, z) dk}{\int E(k, z) dk}, \quad (23)$$

where  $E(k, z)$  is the power spectrum of the velocity field with  $\mathbf{u}^2(z) = \int E(k, z) dk$ .

In general the total thermal diffusivity is given by

$$\chi_{\text{eff}}(\mathbf{x}) = \chi_{\text{SGS}} + \chi(\mathbf{x}). \quad (24)$$

However, in all of the current simulations  $\chi \ll \chi_{\text{SGS}}$  in the CZ such that the Prandtl and Péclet numbers based on  $\chi_{\text{eff}}$  differ very little from  $\text{Pr}_{\text{SGS}}$  and  $\text{Pe}_{\text{SGS}}$ . The Rayleigh number is defined as

$$\text{Ra} = \frac{gd^4}{\nu\chi} \left( -\frac{1}{c_P} \frac{ds}{dz} \right)_{\text{hs}}, \quad (25)$$

which varies as a function of height and is quoted near the surface at  $z/d = 0.85$ . The Rayleigh number in the hydrostatic, non-convecting, state is measured from a one-dimensional model that is run to thermal equilibrium, and where the convectively unstable layer is confined to the near-surface layers (Brandenburg 2016); see also Figure 1. In the hydrostatic case  $\chi = \chi(z)$  and  $\chi_{\text{SGS}}$ , which affects only the fluctuations, plays no role. The turbulent Rayleigh number is quoted from the statistically stationary state using the horizontally averaged mean state,

$$\text{Ra}_t = \frac{gd^4}{\nu \overline{\chi}_{\text{eff}}} \left( -\frac{1}{c_P} \frac{d\overline{s}}{dz} \right) \Big|_{z/d=0.85}, \quad (26)$$

where the overbar denotes temporal and horizontal averaging.

Rotational influence on the flow is measured by several versions of the Coriolis number. First, the global Coriolis number is defined as

$$\text{Co} = \frac{2\Omega_0}{u_{\text{rms}} k_1}, \quad (27)$$

where  $k_1 = 2\pi/d$  is the wavenumber corresponding to the system scale. This definition neglects the changing length scale as a function of rotation and overestimates the rotational influence when rotation is rapid and the convective scale is smaller. A definition that takes the changing length scale into account is given by the vorticity-based Coriolis number

$$\text{Co}_\omega = \frac{2\Omega_0}{\omega_{\text{rms}}}, \quad (28)$$

where  $\omega_{\text{rms}}$  is the volume-averaged rms-value of the vorticity  $\boldsymbol{\omega} = \nabla \times \mathbf{u}$ . Another definition of the Coriolis number taking into account the changing integral length scale is given by

$$\text{Co}_\ell = \frac{2\Omega_0 \ell}{u_{\text{rms}}}, \quad (29)$$

where  $\ell = (\overline{k_{\text{mean}}})^{-1}$  where the overbar denotes averaging over time and CZ. This is a commonly used choice in simulations of convection in spherical shells (Schinnerer et al. 2012; Gastine et al. 2014); see also Aurnou et al. (2020) who considered convection in the limits of slow rotation and rapid rotation.

Let us further define a flux Coriolis number  $\text{Co}_F^2$  as

$$\text{Co}_F \equiv \frac{2\Omega_0 H_p}{u_{\text{flux}}} = 2\Omega_0 H_p \left( \frac{\rho_\star}{F_{\text{bot}}} \right)^{1/3}, \quad (30)$$

where  $u_{\text{flux}}$  is a reference velocity obtained from

$$F_{\text{tot}} = \rho_\star u_\star^3, \quad (31)$$

where  $\rho_\star$  is a reference density, taken here at the bottom of the CZ.  $u_{\text{flux}}$  does not, and does not need to, correspond to any actual velocity and it rather represents the available energy flux. Therefore  $\text{Co}_F$  does not depend on any dynamical flow speed or length scale which are set by complicated interactions of convection, rotation, magnetism, and other relevant physics. On the other hand,  $\text{Co}_F$  depends only on quantities that can either be measured ( $F_{\text{tot}}$ ,  $\Omega_0$ ) or deduced from stellar structure models with relatively little ambiguity ( $H_p$ ,  $\rho_\star$ ). The significance of  $\text{Co}_F$  is seen when rearranging Eq. (20) to yield

$$(2\Omega_0 H_p)^3 \frac{\rho}{F_{\text{bot}}} = (\text{Ra}_F^\star)^{-1}. \quad (32)$$

<sup>2</sup> The same quantity was referred to as stellar Coriolis number in Käpylä (2023).

Identifying the lhs with  $\text{Co}_F^3$ , Eq. (30), gives

$$\text{Co}_F = (\text{Ra}_F^\star)^{-1/3}. \quad (33)$$

An often used phrase in the context of convection simulations targeting the Sun is that while all the other system parameters are beyond the reach of current simulations, the rotational influence on the flow can be reproduced (e.g. Käpylä et al. 2023). Equation (33) gives this a more precise meaning in that the solar value of  $\text{Ra}_F^\star$  needs to be matched by any simulation claiming to model the Sun.

The net vertical energy flux consists of contributions due to radiative diffusion, enthalpy, kinetic energy flux, and viscous fluxes as well as the surface cooling:

$$\overline{F}_{\text{rad}} = -\overline{K} \frac{d\overline{T}}{dz}, \quad (34)$$

$$\overline{F}_{\text{enth}} = c_P \overline{(\rho u_z)' T'}, \quad (35)$$

$$\overline{F}_{\text{kin}} = \frac{1}{2} \overline{\rho \mathbf{u}^2 u_z'}, \quad (36)$$

$$\overline{F}_{\text{visc}} = -2\nu \overline{\rho u_i S_{iz}}, \quad (37)$$

$$\overline{F}_{\text{cool}} = -\int_{z_{\text{bot}}}^{z_{\text{top}}} \overline{C} dz. \quad (38)$$

Here the primes denote fluctuations and overbars horizontal averages. The total convected flux (Cattaneo et al. 1991) is the sum of the enthalpy and kinetic energy fluxes:

$$\overline{F}_{\text{conv}} = \overline{F}_{\text{enth}} + \overline{F}_{\text{kin}}, \quad (39)$$

which corresponds to the convective flux in, for example, mixing length models of convection.

Another useful diagnostic is buoyancy or Brunt-Väisälä frequency, which is given by

$$N^2 = \frac{g}{c_P} \frac{ds}{dz}, \quad (40)$$

and describes the stability of an atmosphere with respect to buoyancy fluctuations if  $N^2 > 0$ . Finally, the Richardson number related to rotation in the stably stratified layers is defined as

$$\text{Ri}_\Omega = \frac{N^2}{\Omega_0^2}. \quad (41)$$

Averages denoted by overbars are typically taken over the horizontal directions and time, unless specifically stated otherwise.

### 3. Results

Three sets of simulations with varying  $\mathcal{F}_n$  and approximately the same values of  $\text{Co}_F$  are presented. These will be referred to as Sets A, B, and C. The non-rotating runs in these sets correspond respectively to Runs K3, K4, and K5 in Käpylä (2019) in terms of  $\mathcal{F}_n$ , although lower values of  $\nu$  and  $\chi_{\text{SGS}}$  were used in the runs of the present study. Note that when  $\mathcal{F}_n$  is varied between the sets of simulations, the rotation rate  $\Omega_0$ , and the diffusivities  $\nu$  and  $\chi_{\text{SGS}}$  are varied at the same time proportional to  $\mathcal{F}_n^{1/3}$  (see, e.g. Käpylä et al. 2020, and Appendix A for more details). Furthermore, the cooling time  $\tau_{\text{cool}}$  is varied proportional to  $\mathcal{F}_n$ . The current simulations have modest Reynolds and Péclet numbers in comparison to astrophysically relevant parameter regimes (e.g. Ossendrijver 2003; Kupka & Muthsam 2017; Käpylä et al. 2023); see Table 1. Earlier studies from non-rotating convection suggest that results obtained at such modestly turbulent regimes remain robust also at the highest resolutions affordable (Käpylä 2021). This is due to the fact that



**Table 1.** Summary of the runs.

Run	$Ra_F[10^{13}]$	$Ra_F^*$	Ta	$\mathcal{F}_n[10^{-6}]$	Co	$Co_\omega$	$Co_\ell$	$Co_F$	Re	$Ra_t[10^6]$	$Ri_\Omega^{RZ}$	grid
A0	0.5	—	0	4.6	0.00	0.00	0.00	0.00	38.7	4.1	—	$288^3$
A1	0.5	$2.5 \cdot 10^2$	$1.0 \cdot 10^4$	4.6	0.07	0.02	0.08	0.28	38.9	4.3	$1.4 \cdot 10^4$	$288^3$
A2	0.5	31	$4.0 \cdot 10^4$	4.6	0.13	0.03	0.16	0.55	39.6	4.3	$3.3 \cdot 10^3$	$288^3$
A3	0.5	3.9	$1.6 \cdot 10^5$	4.6	0.26	0.06	0.31	1.04	39.4	4.6	$8.0 \cdot 10^2$	$288^3$
A4	0.5	0.25	$1.0 \cdot 10^6$	4.6	0.63	0.15	0.71	2.38	40.0	5.1	$1.2 \cdot 10^2$	$288^3$
A5	0.5	0.11	$1.7 \cdot 10^6$	4.6	0.82	0.19	0.87	3.04	40.0	5.5	$7.1 \cdot 10^1$	$288^3$
A6	0.5	$3.1 \cdot 10^{-2}$	$4.0 \cdot 10^6$	4.6	1.27	0.29	1.26	4.56	39.8	6.1	30	$288^3$
A7	0.6	$3.9 \cdot 10^{-3}$	$1.6 \cdot 10^7$	4.6	2.62	0.57	2.17	9.17	38.7	7.5	7.5	$288^3$
A8	0.6	$2.5 \cdot 10^{-4}$	$1.0 \cdot 10^8$	4.6	7.21	1.38	3.88	25.1	35.1	10.9	1.2	$288^3$
A9	0.7	$3.0 \cdot 10^{-5}$	$4.0 \cdot 10^8$	4.6	16.5	2.67	6.31	52.9	30.7	16.0	0.32	$288^3$
B0	1.9	—	0	1.8	0.00	0.00	0.00	0.00	38.3	4.4	—	$288^3$
B1	1.9	$2.5 \cdot 10^2$	$1.0 \cdot 10^4$	1.8	0.07	0.02	0.08	0.27	38.5	4.4	$2.5 \cdot 10^4$	$288^3$
B2	1.9	32	$4.0 \cdot 10^4$	1.8	0.13	0.03	0.17	0.54	38.9	4.5	$6.2 \cdot 10^3$	$288^3$
B3	1.8	4.0	$1.6 \cdot 10^5$	1.8	0.26	0.06	0.32	1.03	39.0	4.8	$1.5 \cdot 10^3$	$288^3$
B4	1.8	0.26	$1.0 \cdot 10^6$	1.8	0.65	0.15	0.70	2.34	39.3	5.3	$2.2 \cdot 10^2$	$288^3$
B5	1.8	$9.3 \cdot 10^{-2}$	$2.0 \cdot 10^6$	1.8	0.90	0.20	0.97	3.21	39.4	5.7	$1.1 \cdot 10^2$	$288^3$
B6	1.8	$3.2 \cdot 10^{-2}$	$4.0 \cdot 10^6$	1.8	1.30	0.29	1.27	4.49	39.1	6.3	55	$288^3$
B7	1.9	$4.0 \cdot 10^{-3}$	$1.6 \cdot 10^7$	1.8	2.69	0.56	2.09	8.98	37.7	7.8	14	$288^3$
B8	2.0	$2.6 \cdot 10^{-4}$	$1.0 \cdot 10^8$	1.8	7.32	1.36	3.90	24.4	34.6	11.4	2.3	$288^3$
B9	2.2	$3.1 \cdot 10^{-5}$	$4.0 \cdot 10^8$	1.8	16.6	2.67	6.32	51.4	30.5	16.2	0.58	$288^3$
C0	5.0	—	0	0.9	0.00	0.00	0.00	0.00	38.1	4.7	—	$288^3$
C1	5.0	$2.6 \cdot 10^2$	$1.0 \cdot 10^4$	0.9	0.07	0.01	0.08	0.27	38.2	4.8	$4.0 \cdot 10^4$	$288^3$
C2	4.9	32	$4.0 \cdot 10^4$	0.9	0.13	0.03	0.16	0.53	38.4	4.9	$9.8 \cdot 10^3$	$288^3$
C3	4.8	4.0	$1.6 \cdot 10^5$	0.9	0.26	0.06	0.31	1.01	38.7	5.0	$2.3 \cdot 10^3$	$288^3$
C4	4.7	0.26	$1.0 \cdot 10^6$	0.9	0.65	0.14	0.73	2.31	39.2	5.5	$3.5 \cdot 10^2$	$288^3$
C5	4.7	$1.2 \cdot 10^{-1}$	$1.7 \cdot 10^6$	0.9	0.84	0.19	0.91	2.96	39.1	5.7	$2.1 \cdot 10^2$	$288^3$
C6	4.7	$3.2 \cdot 10^{-2}$	$4.0 \cdot 10^6$	0.9	1.31	0.28	1.27	4.47	38.7	6.3	87	$288^3$
C7	4.8	$4.1 \cdot 10^{-3}$	$1.6 \cdot 10^7$	0.9	2.71	0.55	2.14	8.93	37.3	8.1	22	$288^3$
C8	5.0	$2.6 \cdot 10^{-4}$	$1.0 \cdot 10^8$	0.9	7.43	1.35	4.03	23.8	34.1	11.6	3.5	$288^3$
C9	5.3	$3.2 \cdot 10^{-5}$	$4.0 \cdot 10^8$	0.9	16.8	2.65	6.44	50.5	30.1	16.7	0.91	$288^3$
A1m	1.1	$2.5 \cdot 10^2$	$4.0 \cdot 10^4$	4.6	0.06	0.01	0.07	0.29	83.2	20.6	$1.4 \cdot 10^4$	$576^3$
A3m	1.0	3.9	$6.4 \cdot 10^5$	4.6	0.24	0.04	0.27	1.05	84.3	21.1	$8.0 \cdot 10^2$	$576^3$
A5m	1.1	0.12	$6.8 \cdot 10^6$	4.6	0.79	0.14	0.78	3.00	83.3	23.1	71	$576^3$
A6m	1.1	$3.2 \cdot 10^{-2}$	$1.6 \cdot 10^7$	4.6	1.21	0.21	1.08	4.53	83.5	24.8	30	$576^3$
A7m	1.1	$4.0 \cdot 10^{-3}$	$6.4 \cdot 10^7$	4.6	2.50	0.40	1.88	9.06	81.1	31.6	7.5	$576^3$
A8m	1.2	$2.5 \cdot 10^{-4}$	$4.0 \cdot 10^8$	4.6	6.83	0.99	3.51	24.8	74.2	45.4	1.2	$576^3$
A9m	1.3	$3.1 \cdot 10^{-5}$	$1.6 \cdot 10^9$	4.6	15.5	1.96	5.59	53.6	65.6	59.5	0.31	$576^3$
A5h	2.1	0.11	$2.7 \cdot 10^7$	4.6	0.76	0.10	0.68	3.00	174	91.4	71	$1152^3$
A9h	2.5	$3.0 \cdot 10^{-5}$	$6.4 \cdot 10^9$	4.6	14.2	1.43	8.36	54.5	143	245	0.31	$1152^3$

**Notes.** Summary of the runs.  $Pr_{SGS} = 1$  in all runs such that  $Pe_{SGS} = Re$ . Runs with rotation were made with  $\theta = 0$ , corresponding to the north pole of the star.  $\tau_{cool} = 2.5(\mathcal{F}_n/\mathcal{F}_n^A)\sqrt{d/g}$ , where  $\mathcal{F}_n^A = 4.6 \cdot 10^{-6}$  is the normalized flux in the runs in Set A.

the main energy transport mechanism (convection) and the main driver of convection (surface cooling) are not directly coupled to the diffusivities. However, the current cases with rotation are more complicated because the supercriticality of convection decreases with increasing rotation rate (e.g. Chandrasekhar 1961; Roberts 1968). The effects of decreasing supercriticality are not studied systematically here, but subsets of the runs in Set A were repeated with higher resolutions ( $576^3$  and  $1152^3$ ) and correspondingly higher  $Ra_F$ ,  $Re$ , and  $Pe$ ; see Sets Am and Ah in Table 1.

### 3.1. Hydrostatic solution

Earlier studies have shown that a purely radiative hydrostatic solution with the Kramers opacity law is a polytrope with in-

dex  $n_{rad} = 3.25$  (Barekat & Brandenburg 2014; Brandenburg 2016). Such a solution arises in the case where  $K = \text{const.}$  and  $\nabla_z T = \text{const.}$  To see if this configuration is recovered with the current set-up, Equations (1) to (3) were solved numerically in a one-dimensional  $z$ -dependent model with otherwise the same parameters as in the 3D simulations corresponding to the runs in Set A. The resulting temperature profile is shown in Fig. 1(a) along with a corresponding horizontally averaged profile from convecting Runs A0, A6, and A9. The stratification is consistent with a polytrope corresponding to  $n_{rad}$  up to a height of roughly  $z/d = 0.75$ . Near the nominal surface of the convection zone,  $z/d = 1$ , the temperature gradient steepens sharply because the cooling term relaxes the temperature toward a constant ( $z$ -independent) value near the surface. Therefore, neither  $K$  nor  $\nabla_z T$  are constants in this transition region between the

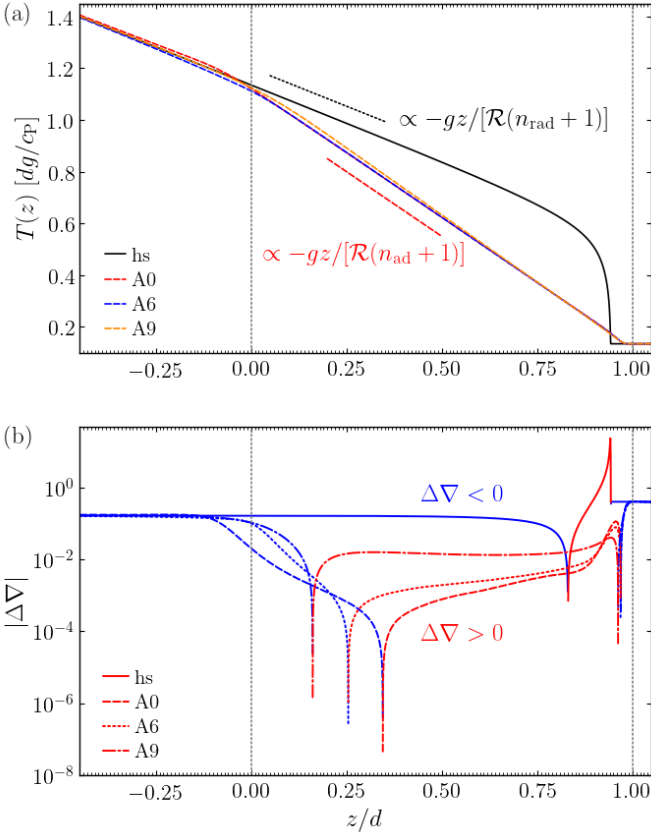


**Fig. 1.** (a) Temperature as a function of height from a 1D hydrostatic model (black solid line) as well as convective runs Run A0 (red dashed), A6 (blue dashed), and A9 (orange dashed). The black (red) dotted line shows a polytropic gradient corresponding to index  $n_{\text{rad}} = 3.25$  ( $n_{\text{ad}} = 1.5$ ) for reference. (b) Absolute value of the superadiabatic temperature gradient  $\Delta\nabla$  from the same runs as indicated by the legend. Red (blue) indicates convectively unstable (stable) stratification. The dotted vertical lines at  $z = 0$  and  $z/d = 1$  denote the base and top of the initially isentropic layer.

radiative and the cooling layers. In the initial state the stratification is isothermal above  $z/d = 1$ , but because the cooling profile  $f_{\text{cool}}$  has a finite width, cooling also occurs below  $z/d = 1$  and the isothermal layer is wider in the final thermally saturated state. This also depends on the value of  $\tau_{\text{cool}}$ . In the convective runs the stratification is nearly polytropic with index  $n_{\text{rad}}$  near the base of the radiative layer and nearly isentropic with  $n_{\text{ad}}$  in the bulk of the convection zone.

The superadiabatic temperature gradient is defined as

$$\Delta\nabla \equiv \nabla - \nabla_{\text{ad}} = -\frac{H_p}{c_p} \frac{ds}{dz}, \quad (42)$$

where  $\nabla = d \ln \bar{T} / d \ln \bar{p}$  is the logarithmic temperature gradient and  $\nabla_{\text{ad}} = 1 - 1/\gamma$  is the corresponding adiabatic gradient. Comparison of the hydrostatic profile and the non-rotating convective model A0 shows that the convectively unstable layer in the former is much thinner than in the latter. This is a direct consequence of the strong temperature and density dependence of the Kramers opacity law. A similar conclusion applies also to the Sun, where the hypothetical non-convecting hydrostatic equilibrium solution has a very thin superadiabatic layer (Brandenburg 2016). The steepness of the temperature gradient near the surface is characterized by the maximum value of  $(\Delta\nabla)_{\text{hyd}}$ , which

is 23.4. By comparison, in the convective Run A0  $\Delta\nabla = 0.12$ . The Rayleigh number – measured at  $z/d = 0.85$  – in the hydrostatic case is  $\text{Ra} = 5.4 \cdot 10^7$ , which is about an order of magnitude greater than  $\text{Ra}_t$  in Run A0.

### 3.2. Qualitative flow characteristic as a function of rotation

Figure 2 shows representative flow fields from runs with slow, intermediate, and rapid rotation, corresponding to Coriolis numbers 0.13, 1.3, and 16.5, respectively. The effects of rotation are hardly discernible in the slowly rotating case A2 with  $\text{Co} = 0.13$ . In the run with intermediate rotation, Run A6 with  $\text{Co} = 1.3$ , the convection cells are somewhat smaller than in the slowly rotating case and more vortical structures are visible near the surface. For the most rapidly rotating case, Run A9 with  $\text{Co} = 16.5$ , the size of the convection cells is drastically reduced in comparison to the other two runs and clear alignment of the convection cells with the rotation vector is seen.

### 3.3. Convective scale as function of rotation

Power spectra  $E(k)$  of the velocity fields for the runs in Set A are shown in Fig. 3 from depths near the surface, at the middle and near the base of the CZ. As was already evident from visual inspection of the flow fields, the dominant scale of the flow decreases as the rotation rate increases. Quantitatively, the wavenumber  $k_{\text{max}}$ , where  $E(k)$  has its maximum, increases roughly in proportion to  $\text{Co}^{1/2}$ . The mean wavenumber  $k_{\text{mean}}$ , computed from Eq. (23), shows the same scaling for  $\text{Co} \gtrsim 2$ . This is explained by the broader distribution of power at different wavenumbers at slow rotation in comparison to the rapid rotation cases where fewer – or just a single – convective modes are dominant; see Figure 3.

A decreasing length scale of the onset of linear instability under the influence of rotation was derived in (Chandrasekhar 1961) with  $k_{\text{onset}} \propto \text{Ta}^{2/3}$ . With  $\text{Ta} \propto \text{Co}^2 \text{Re}^2$ , and with  $\text{Re}$  being approximately constant,  $k_{\text{onset}} \propto \text{Co}^{1/3}$  is obtained. On the other hand, considering the CI part of the CIA balance in the Navier–Stokes equation gives (e.g. Aurnou et al. 2020, see Eq. (A.10) in Appendix A) gives

$$\left(\frac{k_{\text{max}}}{k_1}\right)^2 \propto \frac{2\Omega}{k_1 u} = \text{Co}, \quad (43)$$

or  $k_{\text{max}} \propto \text{Co}^{1/2}$ . This is consistent with the current simulations; see the inset in the left panel of Fig. 3. The same result was obtained in Featherstone & Hindman (2016). Some non-linear convection simulations show scalings that are similar but somewhat shallower than that obtained from the CIA balance; see, e.g., Viviani et al. (2018) and Currie et al. (2020).

To estimate the convective length scale in the Sun based on the current results requires that the value of  $\text{Co}_F$  matches that of the deep solar CZ. The quantities on the rhs of Eq. (30) at the base of the solar convection zone are  $H_p \approx 5 \cdot 10^7$  m,  $\rho_* \approx 200$  kg m $^{-3}$ ,  $F_{\text{bot}} = L_\odot / (4\pi r_{\text{CZ}}^2) \approx 1.27 \cdot 10^8$  kg s $^{-3}$ , with  $r_{\text{CZ}} = 0.7R_\odot \approx 4.9 \cdot 10^8$  m and  $L_\odot = 3.83 \cdot 10^{26}$  W, and  $\Omega_\odot = 2.7 \cdot 10^{-6}$  s $^{-1}$ . Inserting this data into Eq. (30) yields  $\text{Co}_F^\odot \approx 3.1$ . The values of  $\text{Co}_F$  are listed for all runs in the eighth column of Table 1. The moderately rotating runs [A,B,C]5 correspond to the rotational constraint at the base of the solar CZ with  $\text{Co}_F = 3.0 \dots 3.2$ . The mean wavenumber  $k_{\text{mean}}/k_1 \approx 7$  in these simulations corresponds to a horizontal scale of  $\ell_{\text{conv}} = L_x(k_1/k_{\text{mean}}) \approx 0.57d$ . The pressure

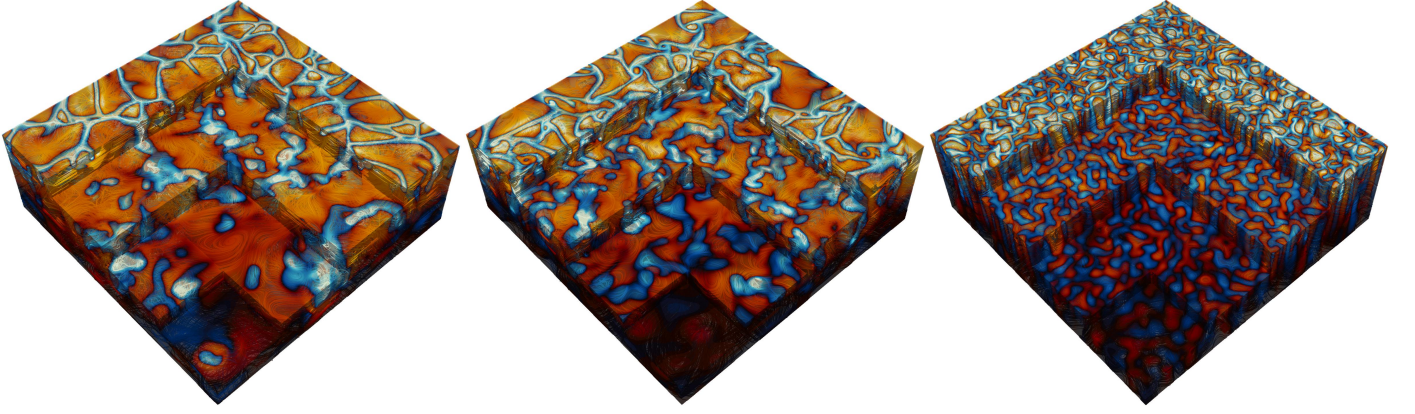


**Fig. 2.** Flow fields from Runs A2 with  $Co = 0.13$  (left), A6 with  $Co = 1.3$  (middle), and A9  $Co = 16.5$  (right) at the north pole ( $\theta = 0^\circ$ ). The colours indicate vertical velocity and the contours indicate streamlines.

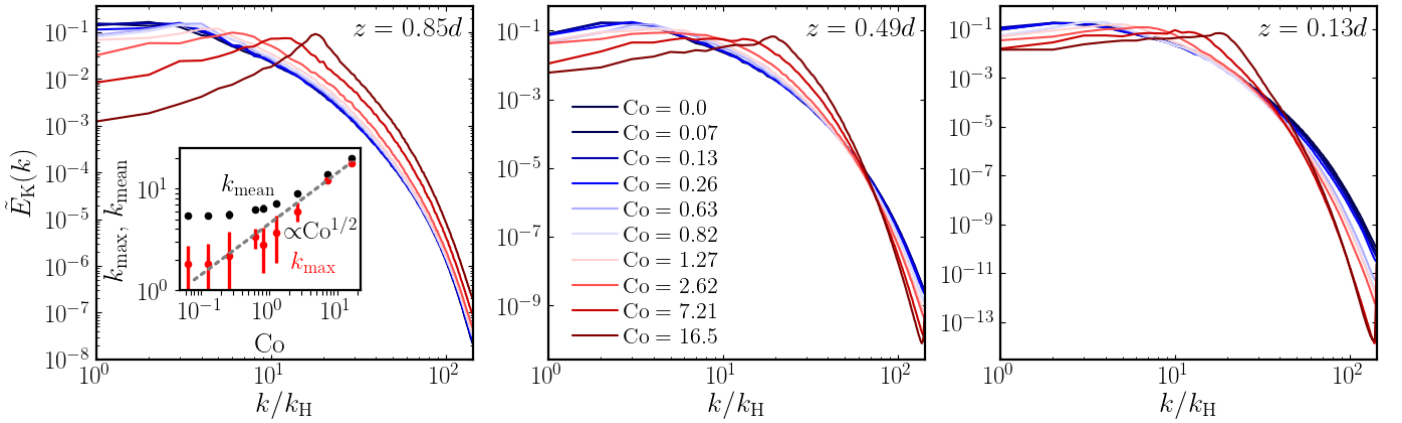


**Fig. 3.** Normalized velocity power spectra near the surface (left panel), middle (middle), and base (right) of the CZ from runs in Set A with  $Co$  varying between 0 and 16.5. The inset in the left panel shows the mean scale  $k_{\text{mean}}$  and wavenumber of the where  $E(k)$  has its maximum ( $k_{\text{max}}$ ) as functions of  $Co$  for  $z/d = 0.85$ . The error bars indicate the standard deviation. The gray dashed line shows a power law proportional to  $Co^{1/2}$ .

scale height at  $z_{\text{DZ}}$  is about  $0.49d$  such that  $\ell_{\text{conv}} \approx 1.16H_{\text{p}}$ . Converting this to physical units using  $H_{\text{p}}^{\odot} \approx 5 \cdot 10^6$  m yields  $\ell_{\text{conv}} \approx 58$  Mm. Following the procedure of Featherstone & Hindman (2016) and using  $k_{\text{max}}$  instead of  $k_{\text{mean}}$ ,  $k_{\text{max}}/k_1 = 3$  and  $\ell_{\text{conv}} \approx 130$  Mm. Both of these estimates are significantly larger than the supergranular scale of  $20 \dots 30$  Mm which was suggested to be the largest convectively driven scale in the Sun by Featherstone & Hindman (2016) and Vasil et al. (2021). On the other hand, a rapidly rotating run of Featherstone & Hindman (2016) with  $\ell_{\text{conv}} \approx 30$  Mm, had Rossby number  $Ro_{\text{FH}} = \tilde{U}/(2\Omega H) = 0.011$ , where  $\tilde{U}$  is a typical velocity amplitude and  $H$  is the shell thickness. This corresponds to a global Coriolis number  $Co = 2\pi Ro_{\text{FH}}^{-1} \approx 14.5$  in the conventions of the current study. In the current runs A9, B9, and C9,  $Co \approx 17$  and  $k_{\text{max}} \approx k_{\text{mean}} \approx 17$ , corresponding to  $\ell_{\text{conv}} \approx 26$  Mm. Therefore the current simulations give a very similar estimate for  $\ell_{\text{conv}}$  at comparable values of  $Co$  despite all of the differences between the model set-ups. However, the values of  $Co_{\text{F}}$  in runs A9, B9, and C9 are at least 16 times higher than in the Sun, suggesting that the simulations of Featherstone & Hindman (2016) were also rotating much faster than the Sun<sup>3</sup>. Therefore

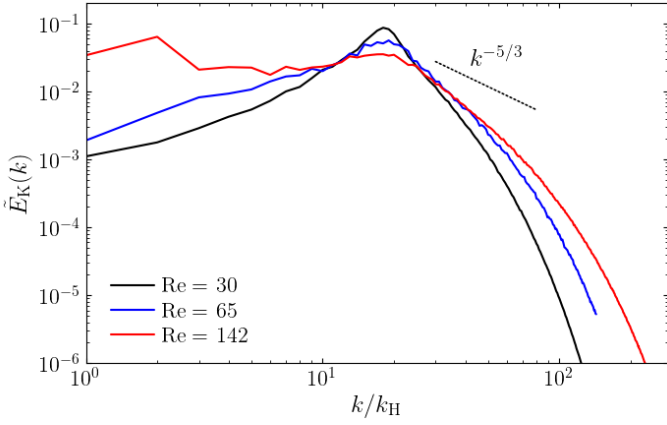
the current results suggest that rotationally constrained convection cannot explain the appearance of supergranular scale as the largest convective scale in the Sun.

Figure 4 shows the velocity power spectra for the most rapidly rotating runs with  $Co \approx 17$  for  $Re = 30 \dots 142$  from Runs A9, A9m, and A9h. There is a marked increase in the power at large scales, which begins to affect  $k_{\text{mean}}$  at the highest  $Re$  or Run A9h. This is due to the gradual onset of large-scale vorticity production, most likely due to two-dimensionalisation of turbulence, that has been observed in various earlier studies of rapidly rotating convection (e.g. Chan 2003, 2007; Chan & Mayr 2013; Käpylä et al. 2011; Guervilly et al. 2014). Despite the rapid rotation with Coriolis numbers exceeding 16, the large-scale vorticity generated in the current simulations is relatively modest apart from Run A9h. A difference to many of the previous studies is that here the relevant thermal Prandtl number ( $Pr_{\text{SGS}}$ ) is of the order of unity whereas in many of the earlier studies  $Pr$  was lower. Large-scale vorticity production was indeed observed in an additional run which is otherwise identical to A9 except that  $Pr_{\text{SGS}} = 0.2$  instead of  $Pr_{\text{SGS}} = 1$  (not shown).

<sup>3</sup> For example, their run with  $Ro = 0.011$  has  $Ra_{\text{F}} = 6.81 \cdot 10^6$ ,  $Ek = 1.91 \cdot 10^{-4}$ , and  $Pr = 1$ , and corresponds to  $Ra_{\text{F}}^* = Ra_{\text{F}} Ek^3 / (8Pr) = 5.9 \cdot 10^{-6}$ , or  $Co_{\text{F}} = (Ra_{\text{F}}^*)^{-1/3} \approx 55$ . This yields

$\Omega/\Omega_{\odot} \approx [(Ra_{\text{F}}^*)_{\odot} / Ra_{\text{F}}^*]^{1/3} \approx 17.6$ , which is approximate because different length scales are used.





**Fig. 4.** Normalized velocity power spectra near the surface of simulations with  $Co \approx 17$  and  $Re = 30 \dots 142$  (Runs A9, A9m, and A9h). The dotted line shows a Kolmogorov  $k^{-5/3}$  scaling for reference.

### 3.4. Measures of rotational influence

#### 3.4.1. Velocity-based $Co$

The suitability of different measures of rotational influence on the flow has been discussed in various works in the literature (e.g. Käpylä 2023). A common – and justified – critique regarding the Coriolis number as defined in Equation (27) is that it does not appreciate the fact that  $l_{conv} = l_{conv}(\Omega)$  (e.g. Vasil et al. 2021). The most straightforward way is to measure the mean wavenumber and use Eq. (29). Figure 5 shows  $Co_\ell$  as a function of  $Co$  for all run listed in Table 1. For slow rotation,  $Co \lesssim 1$ ,  $Co_\ell \propto Co$  because  $u_{conv}$  and  $l_{conv}$  are almost unaffected by rotation. For sufficiently rapid rotation this is no longer true because  $k_{mean} \approx k_{max} \propto Co^{1/2}$  as indicated by Eq. (A.10) and the simulation results; see the inset of Figure 3. This implies that for rapid rotation  $Co_\ell \propto Co^{1/2}$ ; see also Eq. (A.12). This is consistent with the numerical results found in the most rapidly rotating cases; see Fig. 5. The higher resolution runs in Set Am have somewhat lower  $Co_\ell$  than the corresponding runs in Set A because the convective velocities in the higher resolution cases are higher. This shows that the simulations are not yet in an asymptotic regime where the results are independent of the diffusivities. This is further demonstrated by the high resolution runs of Set Ah: Run A5h follows the trend set by Run A5m. The Run A9h with a significantly higher  $Co_\ell$  than in Runs A9 and A9m is explained by the increasing  $k_{mean}$  due to the large-scale vorticity generation in that case. Aurnou et al. (2020) showed that the dynamical Rossby number is related to the diffusion-free modified flux Rayleigh number  $Ra_F^*$ , with different powers for slow and rapid rotation. The corresponding derivations for the Coriolis number  $Co_\ell$  are presented in Appendix A, and which show that  $Co_\ell = (Ra_F^*)^{-1/3}$  (slow rotation) and  $Co_\ell = (Ra_F^*)^{-1/5}$  (rapid rotation). Both scalings are also supported by the simulation results; see the inset of Figure 5.

#### 3.4.2. Vorticity-based $Co$

Another commonly-used definition, Equation (28), is used to take the changing length scale automatically into account. However,  $Co_\omega$  comes with a caveat which has apparently not been discussed hitherto in the astrophysical literature. This is demonstrated by considering a set of rotating systems at asymp-

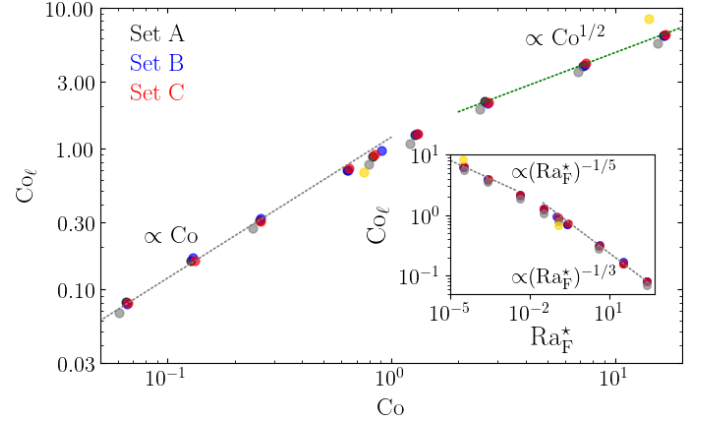


**Fig. 5.** Dynamical Coriolis number  $Co_\ell$  as a function of  $Co$  for all of the runs in Table 1. Power laws proportional to  $Co$  (slow rotation;  $Co < 1$ ) and  $Co^{1/2}$  (rapid rotation;  $Co > 2$ ) are shown for reference. The inset shows  $Co_\ell$  as a function of  $Ra_F^*$  with power laws proportional to  $(Ra_F^*)^{-1/5}$  (rapid rotation;  $Ra_F^* < 3 \cdot 10^{-3}$ ), and  $(Ra_F^*)^{-1/3}$  (slow rotation;  $Ra_F^* > 0.03$ ).

totically high  $Re$  where  $u_{rms}$  is independent of  $Re$ . The forcing is assumed fixed by a constant energy flux through the system, and the asymptotic value of  $u_{rms}$  when  $Re \rightarrow \infty$  as  $u_\infty$ . Furthermore, in this regime the mean kinetic energy dissipation rate

$$\bar{\epsilon}_K = 2\nu\overline{S^2}, \quad (44)$$

where the overbar denotes a suitably defined average, tends to a constant value when normalized by mean length and corresponding rms-velocity (e.g. Sreenivasan 1984; Vassilicos 2015). This value is denoted as  $\epsilon_\infty$ . In low-Mach number turbulence, which is a good approximation of stellar interiors, as well as the current simulations with  $Ma \sim \mathcal{O}(10^{-2})$ ,

$$\bar{\epsilon}_K = \overline{\nu\omega^2} = \nu\omega_{rms}^2. \quad (45)$$

From the definition of system scale Reynolds number it follows that

$$Re = \frac{u_\infty}{\nu k_1} \propto \nu^{-1}, \quad (46)$$

and from Eq. (45) that

$$\omega_{rms} = \left( \frac{\bar{\epsilon}_K}{\nu} \right)^{1/2} = \left( \frac{\epsilon_\infty}{\nu} \right)^{1/2} \propto \nu^{-1/2} \propto Re^{1/2}. \quad (47)$$

Using Eq. (28) it is found that

$$Co_\omega \propto Re^{-1/2}, \quad \text{or} \quad Co \propto Re^{1/2} Co_\omega. \quad (48)$$

This means that  $Co_\omega \rightarrow 0$  as  $Re \rightarrow \infty$  at constant  $Co$ , while the dynamics at large (integral) scales are unaffected. Therefore  $Co_\omega$  underestimates the rotational influence at the mean scale  $k_{mean}$  which dominates the dynamics, as opposed to Eq. (27) overestimating it.

Equation (47) can also be written as

$$\omega_{rms} \equiv k_\omega u_{rms} \propto Re^{1/2}. \quad (49)$$

For sufficiently large  $Re$ , the theoretical prediction is that  $u_{rms} \rightarrow u_\infty = \text{const.}$  and  $k_\omega \propto Re^{1/2}$ . This has been confirmed from numerical simulations of isotropically forced homogeneous turbulence (e.g. Brandenburg & Petrosyan 2012;



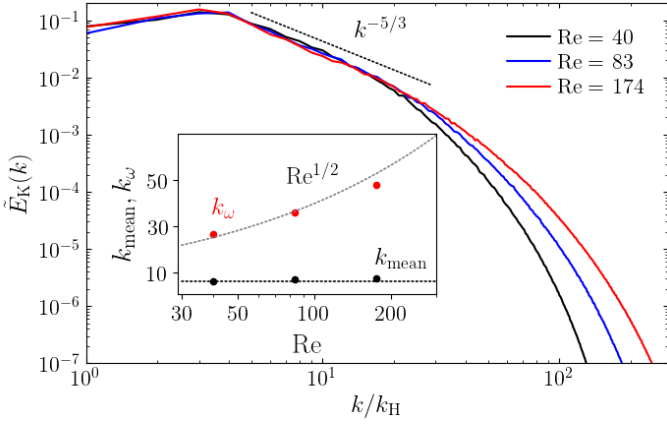


**Fig. 6.** Normalized velocity power spectra near the surface of simulations with  $Co \approx 1.3$  and  $Re = 40 \dots 174$  (Runs A6, A6b, and A6c). The dotted line shows Kolmogorov  $k^{-5/3}$  scaling for reference. The inset shows  $k_{\text{mean}}$  (black symbols) and  $k_\omega$  (red) as functions of  $Re$ . The dotted lines are proportional to powers 0, and  $1/2$  of  $Re$ .

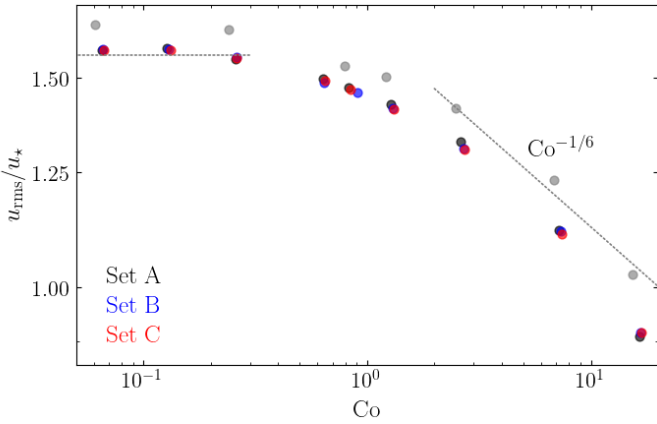


**Fig. 7.** Root-mean-square velocity in the convection zone normalized by  $u_*$ . The dotted line is proportional to  $Co^{1/6}$  as indicated by the theoretical CIA scaling; see Eq. (51).

Candelaresi & Brandenburg 2013). Here the dependence of  $k_\omega$  on  $Re$  is shown in the inset of Figure 6 for runs with  $Co \approx 1.3$  and  $Re$  ranging between 40 and 174. Here the results for  $k_\omega$  fall somewhat below theoretical  $Re^{1/2}$  expectation. This is likely because the asymptotic regime requires still higher Reynolds numbers. On the other hand, the mean wavenumber  $k_{\text{mean}}$  is essentially constant around  $k_{\text{mean}}/k_1 = 7$  in this range of  $Re$  because the dominating contribution to the velocity spectrum come from large scales that are almost unaffected by the increase in  $Re$ .

### 3.5. Convective velocity as a function of total flux and rotation

The scalings of convective velocity as a function of rotation are derived in Appendix A following the same arguments as in Aurnou et al. (2020). For slow rotation the convective velocity depends only on the energy flux:

$$u_{\text{rms}} \sim \left( \frac{F_{\text{tot}}}{\rho} \right)^{1/3} = u_*, \quad (50)$$

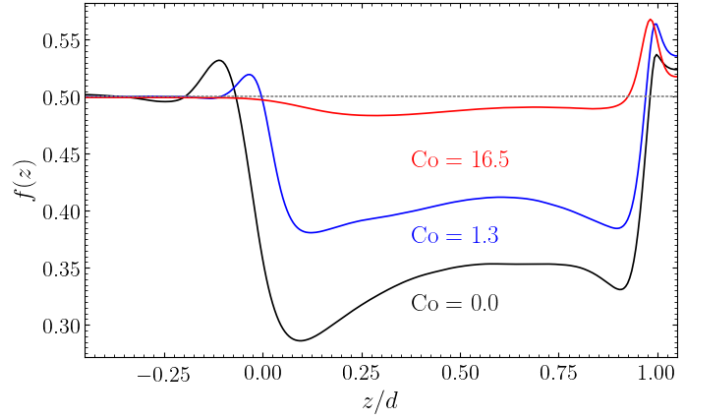


**Fig. 8.** Filling factor of downflows as a function of height  $f(z)$  for three runs with no (black), moderate (blue), and rapid (red) rotation.

where  $u_*$  is defined via Eq. (31). This scaling is altered in the rapidly rotating regime, where

$$u_{\text{rms}} \propto \left( \frac{F}{\rho} \right)^{1/3} Co^{-1/6}. \quad (51)$$

This results agrees with Eq. (50d) Aurnou et al. (2020) and Table 2 of Vasil et al. (2021). Therefore the velocity amplitude in the rapidly rotating regime is expected to depend not only on the available flux but also on rotation. Fig. 7 shows the corresponding numerical results for the Sets A, B, C, and Am. For slow rotation,  $Co \lesssim 0.3$ ,  $u_{\text{rms}}$  is roughly constant around  $u_{\text{rms}} \approx 1.55u_*$  for Sets A, B, and C, and  $u_{\text{rms}} \approx 1.65u_*$  for Set Am. In the rapid rotation regime  $u_{\text{rms}}$  follows a trend which is similar to that indicated in Eq. (51), but the agreement is not perfect. The simulations in this regime may suffer from the fact the supercriticality of convection decreases with  $Co$ . However, the medium resolution runs, visualized by the grey symbols in Fig. 7, do not show a significantly better agreement with theory. Nevertheless, the evidence for CIA balance being reached in the current simulations with rapid rotation is fairly convincing.

### 3.6. Flow statistics

Compressible non-rotating convection is characterized by broad upflows and narrow downflows (Stein & Nordlund 1989; Cattaneo et al. 1991); see also Figure 2. This can be described by the filling factor  $f$  of downflows as

$$\bar{u}_z(z) = f(z)\bar{u}_z^\downarrow + [1 - f(z)]\bar{u}_z^\uparrow(z), \quad (52)$$

where  $\bar{u}_z$  is the mean vertical velocity, whereas  $\bar{u}_z^\uparrow$  and  $\bar{u}_z^\downarrow$  are the corresponding mean up- and downflow velocities. It was shown in Käpylä (2021) that  $f$  is sensitive to the effective Prandtl number of the fluid such that a lower  $Pr$  leads to a lower filling factor. Here a similar study is done as a function of rotation; see Fig. 8. The main result is that  $f$  approaches  $1/2$  in the rapid rotation regime. This is because in rapidly rotating convection the broad upwellings of non-rotating convection are broken up and the flow consist mostly of smaller scale helical columns where the up- and downflows are almost invariant. This is due to the Taylor-Proudman constraint such that derivatives along the rotation axis vanish. Hence the tendency for larger structures to appear at greater depths is inhibited and the average size of convection cells as a function of depth is almost constant; see right-most panel of Figure 2.

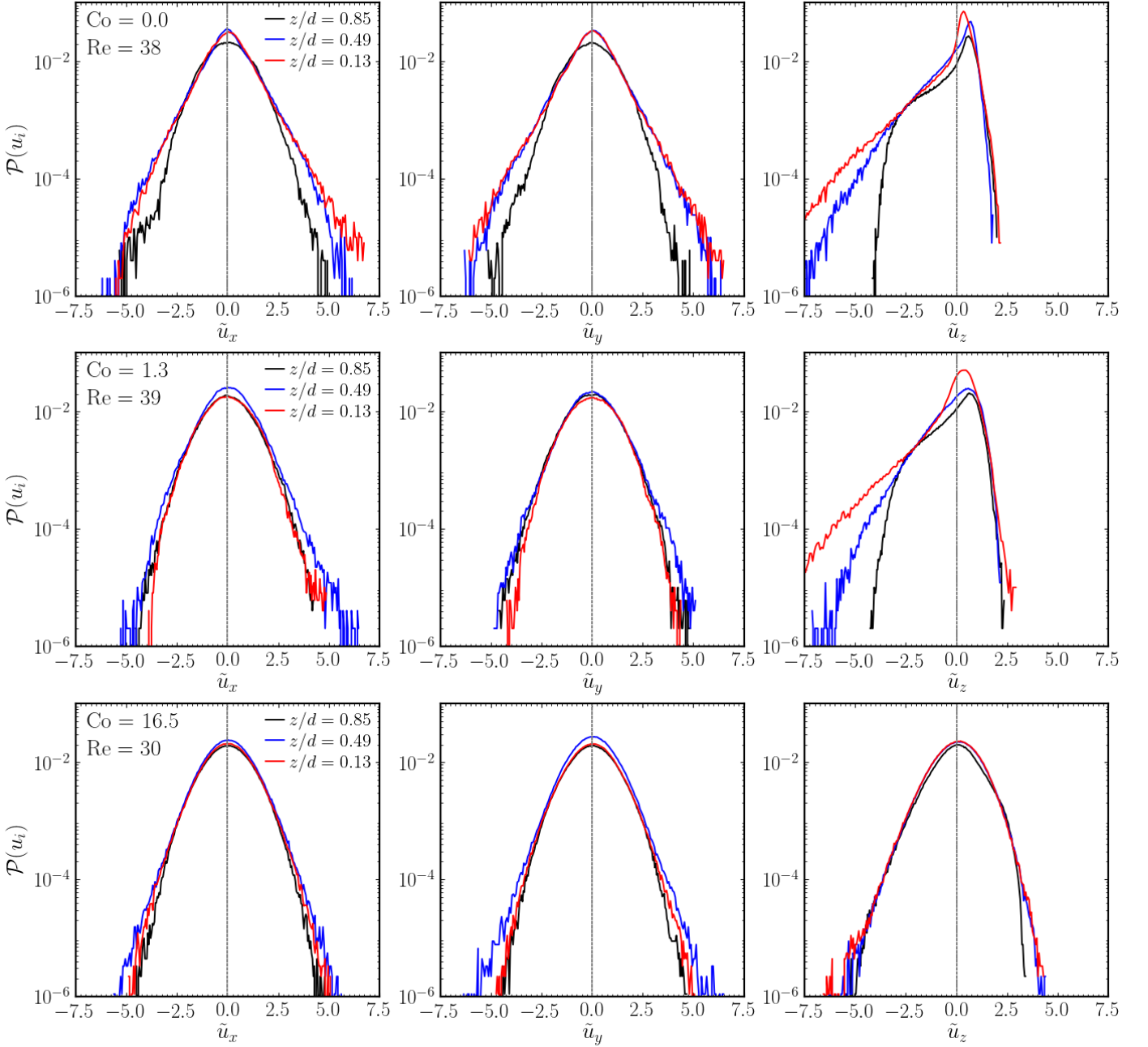


**Fig. 9.** Probability density functions  $\mathcal{P}(u_i)$  for  $u_x$  (left),  $u_y$  (middle), and  $u_z$  (right) for depths  $z/d = 0.85$  (black),  $z/d = 0.49$  (blue), and  $z/d = 0.13$  (red) for runs with  $Co = 0$  (Run A0, top row),  $Co = 1.3$  (Run A6, middle), and  $Co = 16.5$  (Run A9, bottom). The tildes refer to normalization by the respective rms-values.

This is also apparent from the probability density functions (PDFs) of the velocity components  $u_i$ , defined via

$$\int \mathcal{P}(u_i, z) du_i = 1. \quad (53)$$

Figure 9 shows representative examples of PDFs for the extreme cases (Run A0 with  $Co = 0$  and Run A9 with  $Co \approx 16.5$ ) and at an intermediate rotation rate (Run A6,  $Co = 1.3$ ). In non-rotating convection the PDFs of the horizontal components of the velocity are nearly Gaussian near the surface whereas for  $u_z$  the distributions are highly skewed due to the up-/downflow asymmetry. In deeper parts also the horizontal velocities deviate from a Gaussian distribution in agreement with earlier works (e.g. Brandenburg et al. 1996; Hotta et al. 2015; Käpylä 2021)

As the rotation increases the asymmetry of the vertical velocity decreases such that in the most rapidly rotating cases considered here with  $Co \approx 17$ ,  $u_z$  also approaches a Gaussian distribution. Only near the surface ( $z/d = 0.85$ ) a weak asymmetry remains. The horizontal components of velocity continue to have Gaussian distribution as rotation is increased, although there is not enough data to say anything concrete concerning the tails of the distributions at high velocity amplitudes. To further quantify the statistics of the flow, skewness  $\mathcal{S}$  and kurtosis  $\mathcal{K}$  are computed from:

$$\mathcal{S} = \frac{\mathcal{M}^3}{\sigma_u^3}, \quad \mathcal{K} = \frac{\mathcal{M}^4}{\sigma_u^4}, \quad (54)$$

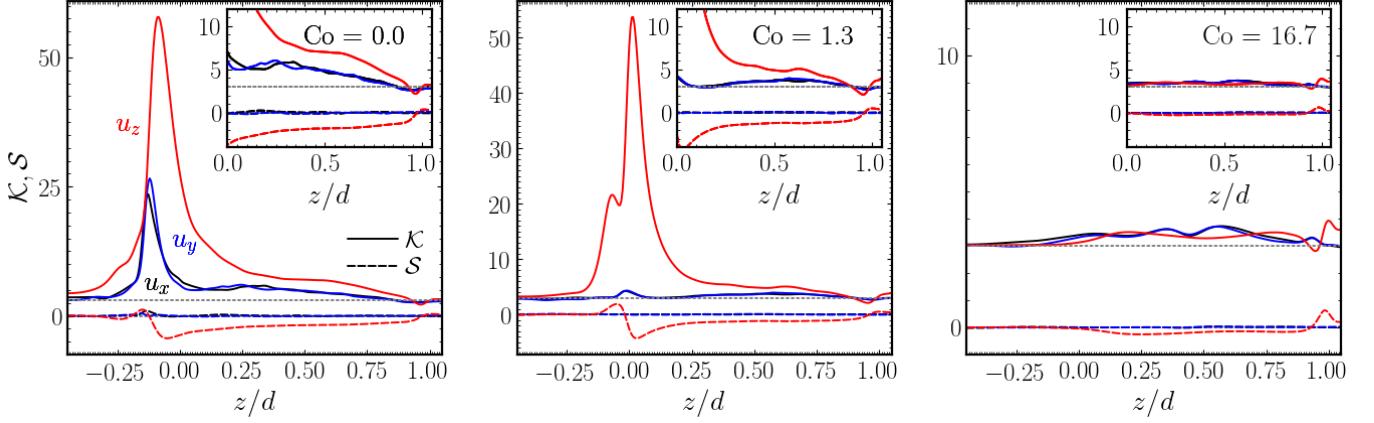


**Fig. 10.** Skewness ( $\mathcal{S}$ , dashed lines) and kurtosis ( $\mathcal{K}$ , solid) from the same runs as in Figure 9. Black, blue, and red colour indicates data corresponding to  $u_x$ ,  $u_y$ , and  $u_z$ , respectively. Note the difference in scale between each of the panels. The insets show a zoom in of the region  $z/d \geq 0$ .

where  $\sigma_u = (\mathcal{M}^2)^{1/2}$ , with

$$\mathcal{M}^n(u_i, z) = \int [u_i(\mathbf{x}) - \bar{u}_i(z)]^n \mathcal{P}(u_i, z) du_i. \quad (55)$$

Figure 10 shows  $\mathcal{S}$  and  $\mathcal{K}$  for all  $u_i$  for the same runs as in Figure 9. The skewness is consistent with zero for the horizontal velocities which is expected as there is not anisotropy in the horizontal plane. The negative values of  $\mathcal{S}$  for  $u_z$  are a signature of the asymmetry between up- and downflows. As rotation is increased,  $\mathcal{S}$  approaches zero also for  $u_z$ . Kurtosis  $\mathcal{K}$  is a measure of non-Gaussianity or intermittency. In the non-rotating case  $\mathcal{K}$  increases from roughly three – indicating Gaussian statistics – to roughly five for horizontal flows as a function of depth within the CZ. For  $u_z$  the increase of  $\mathcal{K}$  is much more dramatic below  $z/d \lesssim 0.3$ . This is because downflows merge at deeper depths such that only a few of them survive deep in the CZ and especially in the overshoot region below roughly  $z = 0$ , where  $\mathcal{K}$  reaches a peak value of roughly 65 for Run A0. A similar, albeit lower, maximum appears also for the horizontal flows. At intermediate rotation (Run A6;  $Co = 1.3$ ),  $u_z$  still exhibits strong intermittency below  $z \approx 0.1$  with  $\max(\mathcal{K}) \approx 54$  whereas  $\mathcal{K}$  for the horizontal flows is significantly reduced in comparison to the non-rotating case. This indicates that especially the vertical flows in this regime are not qualitatively different from those in the non-rotating regime, such that the downflows in the overshoot region are rather abruptly decelerated and diverted horizontally. For the most rapidly rotating case (Run A9;  $Co = 16.5$ ),  $\mathcal{K} \approx 3 \dots 4$  throughout the simulation domain for both vertical and horizontal flows. This is explained by the almost complete wiping out of the up-/downflow asymmetry also in the deep parts of the CZ and in the overshoot region. The absence of a peak in the kurtosis in the overshoot region in the most rapidly rotating cases is likely due to the deeply penetrating vertical flows in those cases due to the unrealistically small Richardson number. This is discussed in more detail in Section 3.7.

The average vertical rms-velocities from the same representative runs as in Figure 9 are shown in Figure 11. The average rms-velocity of the downflows (upflows) is always larger (smaller) than the average total vertical rms-velocity. However, the difference between the up- and downflows and the total rms-velocity diminish monotonically as a function of rotation such that for the most rapidly rotating case the three are almost the

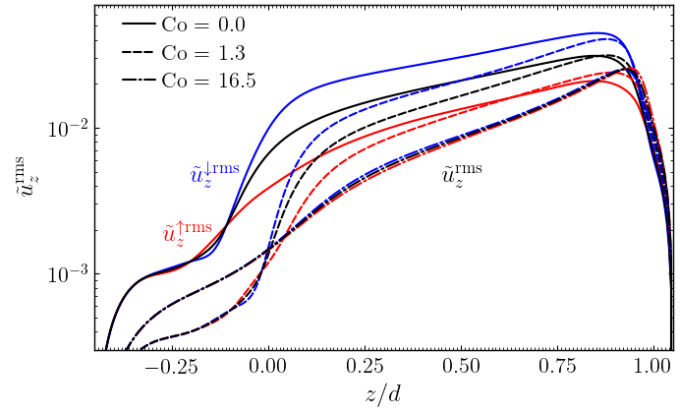


**Fig. 11.** Horizontally averaged vertical rms-velocity for the same runs as in Figure 9. The overall vertical velocity ( $\tilde{u}_z^{\text{rms}}$ ) is shown in black, and the corresponding quantities for up- ( $\tilde{u}_z^{\uparrow, \text{rms}}$ ) and downflows ( $\tilde{u}_z^{\downarrow, \text{rms}}$ ) are shown in red and blue, respectively. The tildes refers to normalization by  $\sqrt{gd}$ .

same. This is another manifestation of the symmetrization of up- and downflows.

Another consequence of the symmetrization of the vertical flows is that the forces on the up- and downflows also approach each other; see Fig. 12, where  $\bar{f}_z = \overline{\rho D u_z / Dt}$ . In accordance with earlier studies (Käpylä et al. 2017; Käpylä 2019), in non-rotating convection the downflows are accelerated near the surface and decelerated roughly when the stratification turns Schwarzschild stable, whereas the upflows are accelerated everywhere except near the surface. This is interpreted such that the upflows are not driven by buoyancy but by pressure forces due to the deeply penetrating downflow plumes. This qualitative picture remains unchanged for slow rotation, but starts to change when  $Co$  is of the order of unity although the region near the surface where the downflows are accelerated is shallower; see Fig. 12(b). For rapid rotation the forces on the up- and downflows are nearly identical. However, the situation continues to qualitatively deviate from the mixing length picture also in the rapidly rotating cases in that the downflows are accelerated only near the surface and braked throughout their descent through the superadiabatic CZ; see Fig. 12(c).

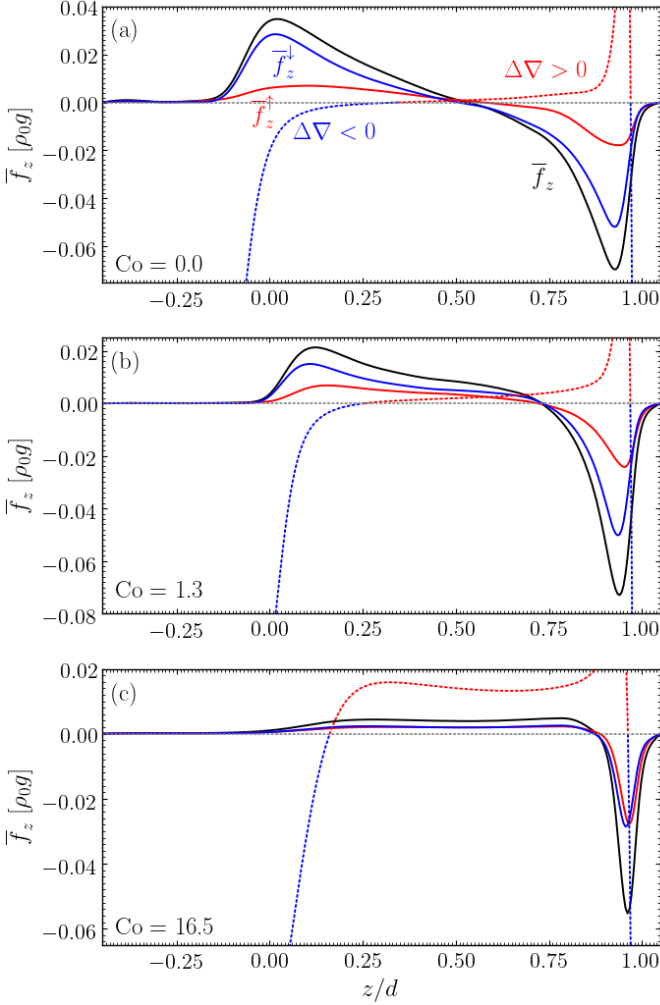


**Fig. 12.** Horizontally averaged total force (black), and separately for up- (red) and downflows (blue). The dotted red/blue line shows the superadiabatic temperature gradient. Data is shown for (a) a non-rotating run A0, (b) an intermediate rotation rate ( $Co = 1.3$ , Run A6), and (c) for rapid rotation ( $Co = 16.5$ , Run A9).

### 3.7. Overshooting and Deardorff layers

The depths of the overshooting and Deardorff layers are studied as functions of rotation using the same definitions of overshooting and Deardorff layers as in previous studies (Käpylä 2019, 2021). The bottom of the CZ is situated at the depth  $z_{CZ}$  where  $\overline{F}_{conv}$  changes from negative to positive with increasing  $z$ . The top of the Deardorff zone (DZ) – or the bottom of the buoyancy zone (BZ) –  $z_{BZ}$ , is where the superadiabatic temperature gradient changes from negative to positive with increasing  $z$ . Then the depth of the DZ is

$$d_{DZ} = \frac{1}{\Delta t} \int_{t_0}^{t_1} [z_{BZ}(t) - z_{CZ}(t)] dt, \quad (56)$$

where  $\Delta t = t_1 - t_0$  is the length of the statistically steady part of the time series. A reference value of the kinetic energy flux ( $\overline{F}_{kin}^{ref}$ ) is measured at  $z_{CZ}$ . The base of the overshoot layer is taken to be the location ( $z_{OS}^{kin}$ ) where  $|\overline{F}_{kin}|$  falls below  $0.01\overline{F}_{kin}^{ref}$ ,

and

$$d_{os}^{kin} = \frac{1}{\Delta t} \int_{t_0}^{t_1} [z_{CZ}(t) - z_{OS}^{kin}(t)] dt, \quad (57)$$

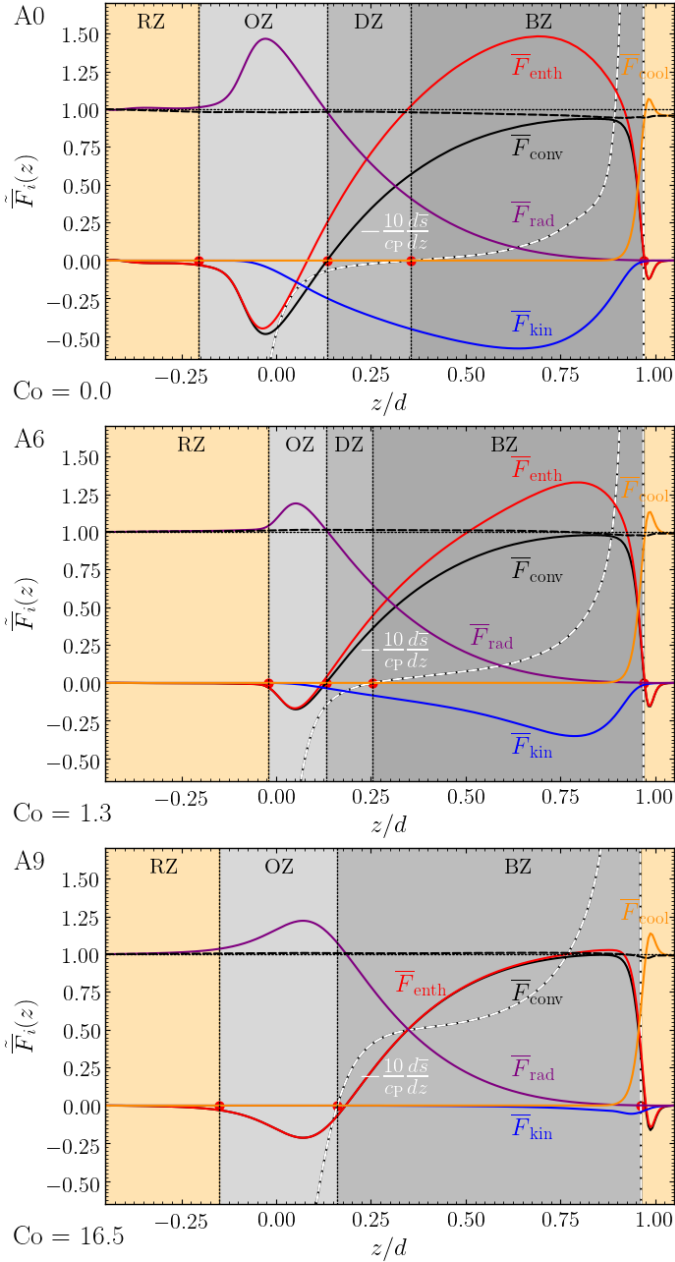
This criterion breaks down in the current models when rotation begins to dominate the dynamics and where  $\overline{F}_{kin} \rightarrow 0$ . Therefore the convected flux  $\overline{F}_{conv}$  was also used to estimate the depth of overshooting. The criterion involving  $\overline{F}_{conv}$  takes the overshoot layer to end at the location ( $z_{OS}^{conv}$ ) where  $|\overline{F}_{conv}|$  falls below  $0.02\overline{F}_{tot}$ . The corresponding overshooting depth ( $d_{os}^{conv}$ ) is computed analogously to Eq. (57). The layer below the OZ is the radiative zone (RZ).

Figure 13 shows the energy fluxes from representative runs at different Coriolis numbers from Set A. For slow and moderate rotation up to  $Co \approx 1$  the situation is qualitatively similar: the positive (upward) enthalpy flux exceeds  $F_{bot}$  in the bulk of the CZ, and it is compensated by a negative (downward) kinetic energy flux  $\overline{F}_{kin}$ . As rotation increases the maxima of  $\overline{F}_{enth}$  and  $|\overline{F}_{kin}|$  decrease monotonically. Similarly, the extents of the overshoot and Deardorff layers diminish with rotation. For the most rapidly rotation case, Run A9 with  $Co = 16.5$ , the kinetic energy flux is almost zero, and  $\overline{F}_{conv} \approx \overline{F}_{enth}$ . This is yet another manifestation of the decreasing asymmetry between the up- and downflows. Moreover, the Deardorff layer vanishes in the rapidly rotating cases.

The positions of the boundaries of the different layers and their depths are summarized for all runs in Table 2, and Fig. 14 shows a summary of the overshooting and Deardorff layer depths as a function of rotation from Sets A, B, and C. The main difference between the sets of simulations is the applied flux  $\mathcal{F}_n$ . The overshooting depth measured from the kinetic helicity flux decreases with increasing rotation as in earlier studies (e.g. Ziegler & Rüdiger 2003; Käpylä et al. 2004). However, the lowermost panel of Fig. 13 shows that the upper part of the radiative layer is mixed far beyond the regions where  $\overline{F}_{kin}$  is non-negligible in the rapidly rotating cases. This is confirmed when the convected flux is used to estimate the overshooting depth. Furthermore,  $d_{os}^{conv}$  increases with rotation for  $Co \gtrsim 1$ . This is explained by the fact that the Mach number, and therefore also the rotation rate  $\Omega_0$ , in the current simulations are much larger than in real stars. This means that the convective, rotation, and Brunt-Väisälä frequencies are closer to each other in the simulations in comparison to, for example, the overshoot region of the Sun. For example, in the most rapidly rotating runs the Richardson number based on the rotation rate  $Ri_\Omega$  is smaller than unity; see the 11th panel of Table 1. This, in addition to the smooth transition from convective to radiative region, can lead gravity waves breaking in the radiative layer, thus contributing to the burrowing of the flows into the RZ (e.g. Lecoanet & Quataert 2013). As a comparison,  $Ri_\Omega$  in the upper part of the solar radiative zone is expected of the order of  $10^4$ . Another possibility is that shear due to the rotationally constrained convective columns lowers the corresponding shear Richardson number close to the limit where turbulence can occur also in thermally stable stratification.

Lowering the luminosity in Sets B and C shows that both measures of  $d_{os}$  decrease with  $\mathcal{F}_n$  in qualitative accordance with earlier results (e.g. Käpylä 2019). Even though  $Ri_\Omega$  is modestly increased in these runs (see the 11th column in Table 1), the most rapidly rotating cases even in the runs with the lowest luminosities continue to show deep mixing which is most likely due to the still unrealistically low  $Ri_\Omega$ . It is numerically very expensive to increase the Richardson number in fully compressible simulations much further, at least without accelerated thermal evolution





**Fig. 13.** Time-averaged mean energy fluxes as defined in Equations (34) to (38) (apart from the negligibly small viscous flux  $\bar{F}_{\text{visc}}$ ) as a functions of  $z$  from Runs A0, A6, and A9. The red circles indicate (from left to right) the bottoms of OZ, DZ, BZ, and the top of the BZ. The grey (orange) shaded areas indicate mixed (radiative) regions.

methods (e.g. Anders et al. 2018, 2020). Comparing the overshooting depths between Runs [A,B,C]5 with solar  $\text{Co}_F$  and the non-rotating Runs [A,B,C]0 shows a reduction between about a third to a half; see the seventh and eighth columns in Table 2. In K pyl  (2019) the overshooting depth extrapolated to the solar value of  $\mathcal{F}_n$  was found to be roughly  $0.1H_p$ , and the current results including rotation reduce this to  $0.05 \dots 0.07H_p$ . However, the dependence of the overshooting depth on  $\mathcal{F}_n$  is here steeper ( $[d_{\text{os}}^{\text{kin}}, d_{\text{os}}^{\text{conv}}] \propto \mathcal{F}_n^{0.15}$ ) than in the nonrotating cases where K pyl  (2019) found  $d_{\text{os}} \propto \mathcal{F}_n^{0.08}$ .

On the other hand, the thickness of the Deardorff layer  $d_{\text{DZ}}$  decreases monotonously as a function of  $\text{Co}$ . In the most rapidly

**Table 2.** Summary of the buoyancy, Deardorff, and overshoot zones.

Run	$z_{\text{BZ}}/d$	$z_{\text{DZ}}/d$	$z_{\text{OS}}^{\text{kin}}/d$	$z_{\text{OS}}^{\text{conv}}/d$	$\tilde{d}_{\text{DZ}}$	$\tilde{d}_{\text{os}}^{\text{kin}}$	$\tilde{d}_{\text{os}}^{\text{conv}}$
A0	0.355	0.134	-0.096	-0.204	0.221	0.230	0.338
A1	0.338	0.128	-0.103	-0.205	0.210	0.231	0.333
A2	0.333	0.124	-0.088	-0.185	0.209	0.212	0.309
A3	0.318	0.130	-0.065	-0.134	0.189	0.195	0.264
A4	0.290	0.131	-0.028	-0.054	0.159	0.159	0.185
A5	0.278	0.132	-0.021	-0.039	0.146	0.153	0.171
A6	0.255	0.131	-0.007	-0.021	0.123	0.138	0.152
A7	0.211	0.134	0.026	-0.025	0.077	0.108	0.159
A8	0.154	0.154	0.065	-0.103	0.001	0.088	0.257
A9	0.161	0.183	0.120	-0.150	0.000	0.064	0.333
B0	0.338	0.124	-0.094	-0.185	0.214	0.218	0.309
B1	0.329	0.121	-0.090	-0.179	0.208	0.211	0.299
B2	0.326	0.117	-0.082	-0.166	0.209	0.200	0.284
B3	0.321	0.124	-0.054	-0.122	0.197	0.179	0.246
B4	0.280	0.125	-0.012	-0.039	0.154	0.138	0.164
B5	0.264	0.124	-0.005	-0.024	0.140	0.128	0.147
B6	0.252	0.125	0.007	-0.009	0.127	0.119	0.134
B7	0.204	0.128	0.036	-0.008	0.076	0.092	0.136
B8	0.138	0.136	0.090	-0.075	0.002	0.046	0.212
B9	0.133	0.156	0.156	-0.126	0.000	0.000	0.281
C0	0.323	0.116	-0.086	-0.166	0.206	0.203	0.283
C1	0.336	0.119	-0.084	-0.166	0.216	0.204	0.285
C2	0.316	0.115	-0.074	-0.150	0.201	0.188	0.265
C3	0.304	0.116	-0.047	-0.105	0.189	0.163	0.221
C4	0.278	0.118	-0.007	-0.031	0.160	0.124	0.149
C5	0.259	0.119	0.001	-0.020	0.140	0.118	0.139
C6	0.240	0.119	0.011	-0.005	0.120	0.108	0.124
C7	0.196	0.121	0.043	-0.002	0.074	0.079	0.124
C8	0.129	0.129	0.106	-0.056	0.000	0.023	0.185
C9	0.118	0.140	0.140	-0.106	0.000	0.000	0.247
A1m	0.321	0.128	-0.101	-0.232	0.193	0.229	0.359
A3m	0.309	0.130	-0.056	-0.143	0.178	0.187	0.274
A5m	0.264	0.133	-0.009	-0.032	0.131	0.143	0.165
A6m	0.250	0.131	-0.002	-0.017	0.119	0.133	0.148
A7m	0.218	0.133	0.018	-0.015	0.085	0.115	0.148
A8m	0.165	0.147	0.064	-0.093	0.018	0.083	0.240
A9m	0.163	0.177	0.052	-0.163	0.000	0.126	0.340
A5h	0.254	0.134	-0.010	-0.031	0.120	0.144	0.165
A9h	0.170	0.170	0.060	-0.183	0.000	0.110	0.353

**Notes.** The tildes for refer to normalization by the pressure scale height at the base of the convection zone.

rotating cases the Deardorff layer vanishes altogether and even reverses such that at the base of the CZ the stratification is unstably stratified but the convective flux is inward; see the lowest panel of Figure 13. This is not significantly changed in more supercritical Runs A9m and A9h. In the entropy rain picture (e.g. Brandenburg 2016) cool material from the surface is brought down deep into otherwise stably stratified layers. This is mediated by relatively few fast downflows with filling factor  $f(z) < 1/2$ , that also produce a strong net downward kinetic energy flux as seen in the top panel of Figure 13; see also Fig. 8, and Table 1 and Sect. 3.3 in Brandenburg (2016). If, on the other hand, the up- and downflows are symmetrized such that  $f(z) = 1/2$  and their velocities are nearly the same,  $\bar{F}_{\text{kin}}$  vanishes and non-local transport due to downflows is no longer significant. Therefore the kinetic energy flux is a proxy of the non-local transport due to downflows and its absence signifies the absence of a Deardorff layer. The depth of the Deardorff layer is

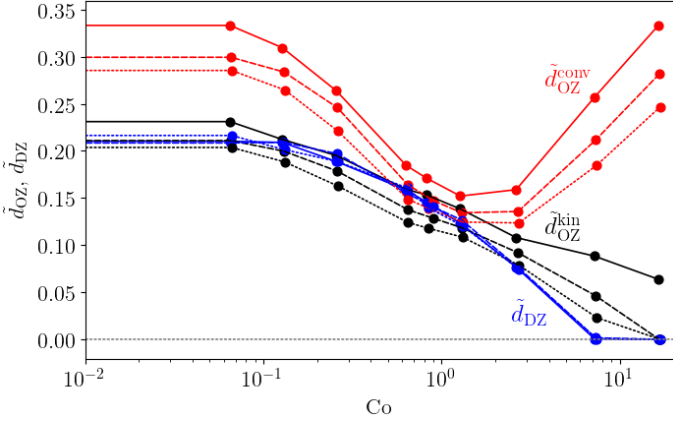


**Fig. 14.** Depth of the overshoot layer from kinetic energy ( $d_{\text{os}}^{\text{kin}}$ ; black lines) and convective fluxes ( $d_{\text{os}}^{\text{conv}}$ ; red), and depth of the Deardorff layer ( $d_{\text{DZ}}$ ; blue) as functions of rotation measured by  $\text{Co}$ . All quantities are normalized by the pressure scale height at the base of the CZ. The different lines correspond to the three different values of  $\mathcal{F}_n$  or Sets A (solid lines), B (dashed), and C (dotted).

independent of the energy flux  $\mathcal{F}_n$ . This further illustrates that the DZ is caused by surface effects which are kept independent of  $\mathcal{F}_n$  in the current simulations. A reduction of  $d_{\text{DZ}}$  of about a third between the non-rotating runs [A,B,C]0 and the runs with the solar value of  $\text{Co}_F$  (Runs [A,B,C]5) was found; see the sixth column of Table 2.

## 4. Conclusions

Simulations of compressible convection were used to study the convective scale and scalings of quantities such as the Coriolis number and convective velocity as functions of rotation. The results were compared to those expected from scalings obtained for incompressible convection with slow and fast rotation (Aurnou et al. 2020). The actual length scale is almost unaffected by rotation for  $\text{Co} \lesssim 1$  and decreases proportional to  $\text{Co}^{1/2}$  for rapid rotation. Correspondingly, the dynamical Coriolis number  $\text{Co}_\ell$  is proportional to  $\text{Co}$  for slow, and  $\propto \text{Co}^{1/2}$  for rapid rotation. Furthermore,  $\text{Co}_\ell$  is proportional to  $(\text{Ra}_F^*)^{-1/3}$  for slow and  $\propto (\text{Ra}_F^*)^{-1/5}$  for rapid rotation, where  $\text{Ra}_F^*$  is the diffusion-free flux-based modified Rayleigh number. Finally, the convective velocity is compatible with proportionality to  $(F_{\text{tot}}/\rho)^{1/3}$  for slow and  $\propto (F_{\text{tot}}/\rho)^{1/3} \text{Co}^{-1/6}$  for rapid rotation. All of these scalings are consistent with those derived by Aurnou et al. (2020) and Vasil et al. (2021). Therefore the simulations seem to follow the CIA scaling at sufficiently rapid rotation.

In an earlier work (Käpylä 2023) several measures were used to characterise the rotational influence on convection. A commonly used definition where the changing length scale of convection is taken into account is  $\text{Co}_\omega = 2\Omega/\omega_{\text{rms}}$ . It is shown that this quantity cannot be used to characterise the effects of rotation on the mean scale because  $\omega_{\text{rms}}$  is expected to increase with the Reynolds number as  $\text{Re}^{1/2}$ . Therefore the only reliable way to account for the changing convective length scale as a function of rotation is to compute the mean wavenumber. This was not correctly identified in Käpylä (2023), and it is now clear that  $\text{Co}_\omega$  will diverge as  $\text{Re}$  increases. On the other hand, Käpylä (2023) introduced a stellar Coriolis number  $\text{Co}_*$  which depends on luminosity and rotation rate which are observable and a reference

density which is available from stellar structure models, but not on any dynamical length or velocity scale. Here this quantity is renamed as  $\text{Co}_F$  and it is furthermore shown that with a suitable choice of length scale,  $\text{Co}_F = (\text{Ra}_F^*)^{-1/3}$ . Matching  $\text{Co}_F$  (or equivalently  $\text{Ra}_F^*$ ) with the target star gives a more concrete meaning to the often-used phrase that it is possible to match the Coriolis number of, for example, the Sun with 3D simulations while most other dimensionless parameters are out of reach (cf. Käpylä et al. 2023).

The current simulations suggest that convection even in the deep parts of the CZ in the Sun is not strongly rotationally constrained and that the CIA balance is therefore inapplicable there. The latter has been argued to be the case by Featherstone & Hindman (2016) and Vasil et al. (2021) to argue that the largest convectively driven scale in the Sun is the supergranular scale. The current results seem to refute this conjecture and that the actual scales may be larger.

Finally, the effects of rotation on convective overshooting and subadiabatic Deardorff zones were studied. The effects of rotation are relatively mild such that for the case with the solar value of  $\text{Co}_F$ , the overshooting depth and the extent of the Deardorff layer are reduced by between 30 and 50 per cent in comparison to the non-rotating case. Therefore the current results suggest an overshooting depth of about five per cent of the pressure scale height at the base of the solar CZ. Taking the current results at face value, a similar depth is estimated for the Deardorff zone. However, the latter is still subject to the caveat that the current simulations do not capture the near-surface layer very accurately and that the driving of entropy rain can be significantly stronger in reality. Another aspect which needs to be revisited in the future is the effect of magnetic fields.

*Acknowledgements.* I thank Axel Brandenburg for his comments on an earlier version of the manuscript. The simulations were performed using the resources granted by the Gauss Center for Supercomputing for the Large-Scale computing project “Cracking the Convective Conundrum” in the Leibniz Supercomputing Centre’s SuperMUC-NG supercomputer in Garching, Germany. This work was supported in part by the Deutsche Forschungsgemeinschaft Heisenberg programme (grant No. KA 4825/4-1).

## References

- Anders, E. H., Brown, B. P., & Oishi, J. S. 2018, *Physical Review Fluids*, 3, 083502
- Anders, E. H., Jermyn, A. S., Lecoanet, D., & Brown, B. P. 2022, *ApJ*, 926, 169
- Anders, E. H. & Pedersen, M. G. 2023, *Galaxies*, 11, 56
- Anders, E. H., Vasil, G. M., Brown, B. P., & Korre, L. 2020, *Physical Review Fluids*, 5, 083501
- Aurnou, J. M., Horn, S., & Julien, K. 2020, *Physical Review Research*, 2, 043115
- Barekat, A. & Brandenburg, A. 2014, *A&A*, 571, A68
- Barker, A. J., Dempsey, A. M., & Lithwick, Y. 2014, *ApJ*, 791, 13
- Bekki, Y., Hotta, H., & Yokoyama, T. 2017, *ApJ*, 851, 74
- Böhm-Vitense, E. 1958, *ZAp*, 46, 108
- Brandenburg, A. 2016, *ApJ*, 832, 6
- Brandenburg, A., Chan, K. L., Nordlund, Å., & Stein, R. F. 2005, *AN*, 326, 681
- Brandenburg, A., Jennings, R. L., Nordlund, Å., et al. 1996, *J. Fluid Mech.*, 306, 325
- Brandenburg, A., Nordlund, Å., & Stein, R. F. 2000, in *Geophysical and Astrophysical Convection*, Contributions from a workshop sponsored by the Geophysical Turbulence Program at the National Center for Atmospheric Research, October, 1995. Edited by Peter A. Fox and Robert M. Kerr. Published by Gordon and Breach Science Publishers, The Netherlands, 2000, p. 85-105, ed. P. A. Fox & R. M. Kerr, 85-105
- Brandenburg, A. & Petrosyan, A. 2012, *Astronomische Nachrichten*, 333, 195
- Brummell, N. H., Clune, T. L., & Toomre, J. 2002, *ApJ*, 570, 825
- Brun, A. S., Strugarek, A., Varela, J., et al. 2017, *ApJ*, 836, 192
- Candelaresi, S. & Brandenburg, A. 2013, *Phys. Rev. E*, 87, 043104
- Cattaneo, F., Brummell, N. H., Toomre, J., Malagoli, A., & Hurlburt, N. E. 1991, *ApJ*, 370, 282
- Chan, K. L. 2003, in *Astron. Soc. Pac. Conf. Ser.*, Vol. 293, *3D Stellar Evolution*, ed. S. Turcotte, S. C. Keller, & R. M. Cavallo, 168

- Chan, K. L. 2007, *Astron. Nachr.*, 328, 1059
- Chan, K. L. & Mayr, H. G. 2013, *Earth and Planetary Science Letters*, 371, 212
- Chandrasekhar, S. 1961, *Hydrodynamic and hydromagnetic stability*
- Christensen, U. R. 2002, *Journal of Fluid Mechanics*, 470, 115
- Christensen, U. R. & Aubert, J. 2006, *Geophys. J. Int.*, 166, 97
- Currie, L. K., Barker, A. J., Lithwick, Y., & Browning, M. K. 2020, *MNRAS*, 493, 5233
- Deardorff, J. W. 1961, *J. Atmosph. Sci.*, 18, 540
- Deardorff, J. W. 1966, *J. Atmosph. Sci.*, 23, 503
- Dobler, W., Stix, M., & Brandenburg, A. 2006, *ApJ*, 638, 336
- Edwards, J. M. 1990, *MNRAS*, 242, 224
- Featherstone, N. A. & Hindman, B. W. 2016, *ApJ*, 830, L15
- Gastine, T., Yadav, R. K., Morin, J., Reiners, A., & Wicht, J. 2014, *MNRAS*, 438, L76
- Greer, B. J., Hindman, B. W., Featherstone, N. A., & Toomre, J. 2015, *ApJ*, 803, L17
- Guervilly, C., Hughes, D. W., & Jones, C. A. 2014, *J. Fluid Mech.*, 758, 407
- Hanasoge, S., Gizon, L., & Sreenivasan, K. R. 2016, *Annual Review of Fluid Mechanics*, 48, 191
- Hanasoge, S. M., Duvall, T. L., & Sreenivasan, K. R. 2012, *Proc. Natl. Acad. Sci.*, 109, 11928
- Hotta, H. 2017, *ApJ*, 843, 52
- Hotta, H., Rempel, M., & Yokoyama, T. 2015, *ApJ*, 803, 42
- Ingersoll, A. P. & Pollard, D. 1982, *Icarus*, 52, 62
- Käpylä, P. J. 2019, *A&A*, 631, A122
- Käpylä, P. J. 2021, *A&A*, 655, A78
- Käpylä, P. J. 2023, *A&A*, 669, A98
- Käpylä, P. J., Browning, M. K., Brun, A. S., Guerrero, G., & Warnecke, J. 2023, *Space Sci. Rev.*, 219, 58
- Käpylä, P. J., Gent, F. A., Olsper, N., Käpylä, M. J., & Brandenburg, A. 2020, *Geophysical and Astrophysical Fluid Dynamics*, 114, 8
- Käpylä, P. J., Korpi, M. J., & Tuominen, I. 2004, *A&A*, 422, 793
- Käpylä, P. J., Mantere, M. J., & Hackman, T. 2011, *ApJ*, 742, 34
- Käpylä, P. J., Rheinhardt, M., Brandenburg, A., et al. 2017, *ApJ*, 845, L23
- Käpylä, P. J., Viviani, M., Käpylä, M. J., Brandenburg, A., & Spada, F. 2019, *Geophysical and Astrophysical Fluid Dynamics*, 113, 149
- Karak, B. B., Miesch, M., & Bekki, Y. 2018, *Physics of Fluids*, 30, 046602
- King, E. M. & Buffett, B. A. 2013, *Earth and Planetary Science Letters*, 371, 156
- Kupka, F. & Muthsam, H. J. 2017, *Liv. Rev. Comp. Astrophys.*, 3, 1
- Lecoanet, D. & Quataert, E. 2013, *MNRAS*, 430, 2363
- O'Mara, B., Miesch, M. S., Featherstone, N. A., & Augustson, K. C. 2016, *Adv. Space Res.*, 58, 1475
- Ossendrijver, M. 2003, *A&A Rev.*, 11, 287
- Pencil Code Collaboration, Brandenburg, A., Johansen, A., et al. 2021, *The Journal of Open Source Software*, 6, 2807
- Proxauf, B. 2021, PhD thesis, Georg August University of Göttingen, Germany
- Roberts, P. H. 1968, *Philosophical Transactions of the Royal Society of London Series A*, 263, 93
- Roxburgh, L. W. & Simmons, J. 1993, *A&A*, 277, 93
- Saikia, E., Singh, H. P., Chan, K. L., Roxburgh, I. W., & Srivastava, M. P. 2000, *ApJ*, 529, 402
- Schrinner, M., Petitdemange, L., & Dormy, E. 2012, *ApJ*, 752, 121
- Schumacher, J. & Sreenivasan, K. R. 2020, *Reviews of Modern Physics*, 92, 041001
- Singh, H. P., Roxburgh, I. W., & Chan, K. L. 1995, *A&A*, 295, 703
- Singh, H. P., Roxburgh, I. W., & Chan, K. L. 1998, *A&A*, 340, 178
- Spruit, H. 1997, *Mem. Soc. Astron. Italiana*, 68, 397
- Sreenivasan, K. R. 1984, *Physics of Fluids*, 27, 1048
- Stein, R. F. & Nordlund, A. 1989, *ApJ*, 342, L95
- Stein, R. F. & Nordlund, Å. 1998, *ApJ*, 499, 914
- Stevenson, D. J. 1979, *Geophysical and Astrophysical Fluid Dynamics*, 12, 139
- Tremblay, P.-E., Ludwig, H.-G., Freytag, B., et al. 2015, *ApJ*, 799, 142
- Vasil, G. M., Julien, K., & Featherstone, N. A. 2021, *Proceedings of the National Academy of Science*, 118, e2022518118
- Vassilicos, J. C. 2015, *Annual Review of Fluid Mechanics*, 47, 95
- Vitense, E. 1953, *ZAp*, 32, 135
- Viviani, M. & Käpylä, M. J. 2021, *A&A*, 645, A141
- Viviani, M., Warnecke, J., Käpylä, M. J., et al. 2018, *A&A*, 616, A160
- Weiss, A., Hillebrandt, W., Thomas, H.-C., & Ritter, H. 2004, *Cox and Giuli's Principles of Stellar Structure* (Cambridge, UK: Cambridge Scientific Publishers Ltd)
- Ziegler, U. & Rüdiger, G. 2003, *A&A*, 401, 433

## Appendix A: Convective scalings as function of rotation

The scalings of relevant dynamical quantities in convection are shortly summarized following the studies of Barker et al. (2014), Aurnou et al. (2020), and Vasil et al. (2021). In the rapidly rotating regime the Coriolis-inertial-Archimedean (CIA) balance is assumed to hold.

### A.1. No or slow rotation ( $Co \ll 1$ )

For slow rotation the convective length scale  $\ell_{\text{conv}}$  is of the order of the pressure scale height  $H_p = -(\partial \ln p / \partial z)^{-1}$ , and the vertical and horizontal extents of convection cells are of the same order of magnitude. When rotation is slow, the dominant balance in the Navier–Stokes equation is between the advection and buoyancy terms:

$$\mathbf{u} \cdot \nabla \mathbf{u} \sim \frac{T'}{T} \mathbf{g} \longrightarrow \frac{u^2}{H} \sim \frac{T'}{T} g, \quad (\text{A.1})$$

where  $H$  is the convective scale  $T'$  is the temperature fluctuation. Assuming that convection transports most of the energy gives

$$F_{\text{tot}} \sim c_p \rho u T', \quad (\text{A.2})$$

and therefore

$$u^3 \sim \frac{gH}{c_p T} \frac{F_{\text{tot}}}{\rho}, \text{ or } u \sim \left( \frac{gH}{c_p T} \right)^{1/3} \left( \frac{F_{\text{tot}}}{\rho} \right)^{1/3}. \quad (\text{A.3})$$

Choosing  $H = c_p T / g$  gives:

$$u \sim \left( \frac{F_{\text{tot}}}{\rho} \right)^{1/3} \equiv u_*, \quad (\text{A.4})$$

where  $u_*$  is a hypothetical velocity that is a measure of the available energy flux. Therefore, for slow rotation,

$$Co = Co_\ell = \frac{2\Omega H}{u} = 2\Omega H \left( \frac{\rho}{F_{\text{tot}}} \right)^{1/3} = (Ra_F^*)^{-1/3}. \quad (\text{A.5})$$

Temperature fluctuation can be computed from the convective flux

$$F_{\text{conv}} = c_p \rho u T', \longrightarrow c_p T' = \frac{F}{\rho u}. \quad (\text{A.6})$$

Using  $u$  from Eq. (A.4) yields:

$$c_p T' = \left( \frac{F}{\rho} \right)^{2/3}. \quad (\text{A.7})$$

### A.2. Rapid rotation ( $Co \gg 1$ )

The CIA balance means that

$$2\Omega_0 \partial_{\parallel} \mathbf{u} \sim \mathbf{u} \cdot \nabla \boldsymbol{\omega} \sim \nabla \times \left( \frac{T'}{T} \mathbf{g} \right), \quad (\text{A.8})$$

which results from the curl of the Navier–Stokes equation (e.g. Aurnou et al. 2020), and where  $\partial_{\parallel}$  is a derivative along the rotation vector. Considering first the CI part of CIA balance gives

$$\mathbf{u} \cdot \nabla \boldsymbol{\omega} \sim 2\Omega \partial_z \mathbf{u} \longrightarrow k_{\perp}^2 u^2 \sim 2\Omega u k_{\parallel}, \quad (\text{A.9})$$

where  $k_{\perp}$  and  $k_{\parallel}$  are the wavenumbers perpendicular and parallel to the rotation vector. Identifying  $k_{\perp}$  as the dominant horizontal scale of convection ( $k_{\max} \sim \ell^{-1}$ ) and  $k_{\parallel}$  as  $k_{\perp} \sim H^{-1}$ , leads to

$$\left(\frac{H}{\ell}\right)^2 \propto \left(\frac{k_{\max}}{k_{\perp}}\right)^2 \propto \frac{2\Omega}{k_{\perp}u} = \text{Co}, \quad \text{or} \quad \frac{\ell}{H} = \text{Co}^{-1/2}. \quad (\text{A.10})$$

Furthermore,

$$\text{Co} = \frac{2\Omega H}{u} = \frac{2\Omega \ell}{u} \frac{H}{\ell} = \text{Co}_{\ell} \text{Co}^{1/2}, \quad (\text{A.11})$$

or

$$\text{Co}_{\ell} = \text{Co}^{1/2}. \quad (\text{A.12})$$

The convective length scale in terms of  $u$  and global quantities is

$$\ell = \left(\frac{Hu}{2\Omega}\right)^{1/2}. \quad (\text{A.13})$$

To derive the convective velocity, CA part of the CIA balance is used:

$$2\Omega_0 \partial_{\parallel} \mathbf{u} \sim \nabla \times \left(\frac{T'}{T} \mathbf{g}\right), \quad \longrightarrow \quad \frac{2\Omega u}{H} \sim \frac{gF_{\text{tot}}}{c_{\text{P}}\rho T u \ell}. \quad (\text{A.14})$$

Substitute  $\ell$  from Eq. (A.13) and rearrange to get:

$$u = \left(\frac{gF_{\text{tot}}}{c_{\text{P}}\rho T}\right)^{2/5} \left(\frac{H}{2\Omega}\right)^{1/5} = \left(\frac{F_{\text{tot}}}{\rho}\right)^{2/5} (2\Omega H)^{-1/5}, \quad (\text{A.15})$$

where  $H = c_{\text{P}}T/g$  was additionally used. This is equivalent to:

$$u = \left(\frac{F_{\text{tot}}}{\rho}\right)^{1/3} \text{Co}^{-1/6}. \quad (\text{A.16})$$

The length scale  $\ell$  is obtained from Eq. (A.14) with substitution of  $u$  from Eq. (A.15):

$$\frac{\ell}{H} = \left(\frac{F_{\text{tot}}}{\rho}\right)^{1/5} (2\Omega H)^{-3/5}, \quad (\text{A.17})$$

where  $H = c_{\text{P}}T/g$  was again used. Now,

$$\text{Co}_{\ell} = \frac{2\Omega \ell}{u} = (2\Omega H)^{3/5} \left(\frac{\rho}{F_{\text{tot}}}\right)^{1/5}. \quad (\text{A.18})$$

Bearing Eq. (20) in mind gives:

$$\text{Co}_{\ell} = \left(\frac{8\Omega^3 H^3 \rho}{F}\right)^{1/5} = (\text{Ra}_{\text{F}}^*)^{-1/5}. \quad (\text{A.19})$$

Finally, the temperature fluctuation using Eq. (A.16) is:

$$c_{\text{P}}T' = \frac{F_{\text{tot}}}{\rho u} = \left(\frac{F_{\text{tot}}}{\rho}\right)^{2/3} \text{Co}^{1/6}. \quad (\text{A.20})$$